

# A Hybrid Discretize-then-Project Reduced Order Model for Turbulent Flows on Collocated Grids with Data-Driven Closure

Nadim Rooholamin<sup>\*1</sup>, Kabir Bakhshaei<sup>†1,2</sup>, and Giovanni Stabile<sup>‡1</sup>

<sup>1</sup>Biorobotics Institute, SMART Lab, Sant'Anna School of Advanced Studies, Pisa, Italy

<sup>2</sup>Department of Computer Science, University of Pisa, Pisa, Italy

## Abstract

This study presents a hybrid reduced-order modeling (ROM) framework for turbulent incompressible flows on collocated finite volume grids. The methodology employs the "discretize-then-project" consistent flux strategy, which ensures mass conservation and pressure-velocity coupling without requiring auxiliary stabilization like boundary control or pressure stabilization techniques. However, because standard Galerkin projection fails to yield physically consistent results for the turbulent viscosity field, a hybrid strategy is adopted: velocity and pressure are resolved via intrusive projection, while the turbulent viscosity is reconstructed using a non-intrusive data-driven closure. We evaluate three neural network architectures, Multilayer Perceptron (MLP), Transformers, and Long Short-Term Memory (LSTM), to model the temporal evolution of the viscosity coefficients. Validated against a 3D Large Eddy Simulation of a lid-driven cavity, the LSTM-based closure demonstrates superior performance in capturing transient dynamics, achieving relative errors of 0.7% for velocity and 4% for turbulent viscosity. The resulting framework effectively combines the mathematical rigor of the consistent flux formulation with the adaptability of deep learning for turbulence modeling.

**Keywords:** ROM, Turbulence, POD-Galerkin, Hybrid Data-Driven Closure, Consistent Flux Method, Finite Volume Method, LSTM, Transformer.

## 1 Introduction

Fluid dynamics represents one of the most intricate and continuously evolving disciplines, characterized by ongoing advancements and a wide spectrum of theoretical investigations and practical applications. It constitutes a branch of fluid mechanics devoted to the analysis of the behavior of liquids and gases in motion. The resolution of a fluid dynamics problem typically entails solving, either analytically or numerically, highly complex differential equations in order to evaluate physical quantities such as velocity, pressure, density, or temperature as functions of spatial coordinates and time. At present, numerical simulations, most notably Computational Fluid Dynamics (CFD), have become the standard approach. CFD is now routinely used for the simulation of complex flow problems; however, its application is often restricted by the considerable computational cost and memory requirements associated with high-resolution models. This issue becomes more severe when turbulent flows are considered, or when the geometry and physics of the problem increase in complexity. For this reason, reduced-order modeling (ROM) approaches have been widely investigated as an alternative strategy to reduce computational effort while still capturing the main flow behavior.

The objective of these methods is to decrease the dimensionality of high-fidelity models, thereby mitigating computational costs while retaining physical accuracy [1, 2]. Reduced order methods can be broadly classified into projection-based approaches and non-projection-based approaches, the latter

---

<sup>\*</sup>nadim.r99@gmail.com

<sup>†</sup>kabir.bakhshaei@santannapisa.it

<sup>‡</sup>giovanni.stabile@santannapisa.it

including truncation methods, goal-oriented techniques, and low-dimensional models constructed from input–output data[3, 4, 5, 6].

Within this framework, projection-based methods achieve dimensionality reduction by projecting the governing partial differential equations (PDEs) onto a lower-dimensional subspace, referred to as the reduced basis (RB) [7, 8, 9]. This results in a compact model that remains consistent with the governing physical laws. Several strategies are commonly employed to construct the reduced basis, including Dynamic Mode Decomposition (DMD), greedy selection procedures, and Proper Orthogonal Decomposition (POD)[10, 11, 12, 13]. These approaches enable the identification of low-dimensional subspaces that retain the dominant features of the original high-fidelity solution. To alleviate the computational effort required by nonlinear operators, several ROM techniques rely on hyper-reduction methods, including gappy POD and discrete empirical interpolation [14, 15, 16, 17, 18].

A classical example of a projection-based technique is the POD–Galerkin method [19]. Initially, POD extracts the most significant modes from a dataset (e.g., snapshots of velocity, pressure, or temperature fields), thereby isolating the principal coherent structures of the flow while discarding less relevant details. Subsequently, the Galerkin projection is utilized to project the governing equations onto the reduced subspace, resulting in a model defined exclusively by the coefficients of the dominant modes [20, 21]. This procedure drastically lowers the number of unknowns compared to the full-order model. While POD–Galerkin methods were first introduced within the context of finite element (FE) discretizations, increasing interest has recently been directed toward their extension to finite volume methods (FVMs), owing to their robustness and their ability to guarantee both local and global conservation properties [22, 23, 24, 25, 26, 27, 28, 29, 30, 31, 32].

In this work, simulations are carried out within the OpenFOAM framework. The solver relies on a finite volume (FV) discretization on collocated grids, which is a common choice in large-scale CFD applications. From a practical standpoint, collocated layouts simplify the implementation of the numerical algorithms and typically require less memory than staggered-grid approaches [33, 34, 35].

Despite their widespread use, FV-based POD–Galerkin reduced-order models may still suffer from numerical instabilities. In incompressible flow settings, these instabilities typically originate from the interaction between convection-dominated transport and the pressure–velocity coupling introduced by the discretization of the Navier–Stokes equations [36, 37, 38, 39, 40, 41]. If not properly addressed, such effects can adversely impact both the accuracy and robustness of the reduced-order approximation.

Several studies on POD–Galerkin ROMs have shown that enforcing a divergence-free reduced velocity space leads to the elimination of the pressure gradient contribution in the reduced momentum formulation. Constructing a velocity-only reduced-order formulation with stable numerical behavior on collocated grids, however, is not straightforward because the discrete divergence and gradient operators do not satisfy the necessary compatibility conditions. As a result, stability usually requires the combined use of Rhie–Chow interpolation at the full-order level and additional pressure stabilization techniques at the reduced level [42, 43, 44, 45, 46, 47, 48].

To obtain reliable velocity and pressure reconstructions, both in FE and FV reduced-order frameworks, two strategies are commonly adopted. One is the supremizer enrichment of the velocity basis, which enforces the inf–sup condition and thereby removes the pressure instabilities that otherwise arise. While effective, this method typically requires a number of supremizer modes equal to or greater than the number of pressure modes, which inevitably increases the dimensionality and online computational cost of the ROM. The second strategy leverages the velocity approximation within the ROM to solve a pressure Poisson equation. Although widely used, this approach raises difficulties in prescribing appropriate boundary conditions for the pressure equation [49, 50, 51, 52, 53, 54, 55].

Several studies have shown that stabilization alone does not necessarily guarantee high accuracy in reduced-order velocity and pressure fields. Compared to direct POD projection of full-order solutions, the resulting errors may increase by one to two orders of magnitude. This limitation has been documented even for canonical non-parametric laminar test cases, including the lid-driven cavity problem [25, 49, 53, 56].

An alternative pressure recovery approach involves using a pressure reduced basis in conjunction with the associated temporal coefficients originally derived for the velocity field to reconstruct the pressure contribution in the momentum equations. This method offers the computational advantage of only requiring the resolution of the momentum system. However, because the pressure field is reconstructed using the exact same set of coefficients as the velocity, this strategy necessitates an identical number of modes for both the velocity and pressure reduced bases, which can impose constraints on

the overall efficiency of the model[20, 24].

More recent developments in the FE community include stabilization via local projection methods and the introduction of an artificial compressibility condition to replace the incompressibility constraint in the Navier–Stokes equations [52, 57, 58, 59].

In this work, building on our earlier study [60], we extend the discretize–then–project strategy to fully three-dimensional turbulent configurations. We consider a reduced-order modelling (ROM) of the incompressible Navier–Stokes equations on collocated grids, for which no pressure stabilization or additional boundary-enforcement procedures are introduced at the reduced level. The approach is formulated directly at the discrete level: the operators of the full-order model (FOM) together with the boundary contributions are projected onto POD-based reduced spaces. This discretize–then–project strategy ensures consistency between the reduced velocity and pressure representations [61, 60].

However, applying the same procedure to the turbulence field does not yield consistent results at the reduced level. As a new novelty to address this, we propose a hybrid approach: the turbulent viscosity is incorporated through a data-driven methodology [61, 62, 63, 64, 65, 66, 67, 68].

Data-driven methods rely on learning from available data rather than prescribing an explicit physical model, often using machine learning techniques to represent the system. Broadly speaking, these methods can be divided into either purely data-driven or physics-informed data-driven approaches. In this work, we adopt a purely data-driven strategy to model the non-intrusive path of our hybrid framework, with the objective of evaluating the consistency of the reconstructed turbulence field. Specifically, we investigate and compare three different neural network architectures, Multilayer Perceptron (MLP), Transformers, and Long Short-Term Memory (LSTM) networks, to predict the temporal evolution of the eddy viscosity coefficients. This allows us to identify the most suitable model for capturing the complex, transient nonlinear interactions inherent in 3D turbulent flows[69].

This work adopts a POD–Galerkin reduced order modeling framework following a ”discretize-then-project” strategy. As detailed in the sources, the strategy approach is fundamentally intrusive, as it requires direct access to the fully discrete system matrices and numerical algorithms of the high-fidelity solver to project the discrete operators onto the reduced basis. The reduced-order model is constructed by directly projecting the fully discrete operators of the full-order model, together with the associated boundary contributions, onto the reduced spaces. This choice allows the reduced system to retain a close correspondence with the original FV formulation, including both linear and nonlinear terms arising from the discretization. The practical implementation of this approach is supported by ITHACA-FV, an open-source library built on top of OpenFOAM that provides direct access to the discrete operators and numerical solvers of the full-order model [68, 70].

The present work builds on the study of Star et al.[60] , but departs from it in several important aspects. In that work, the analysis was restricted to two-dimensional laminar configurations, namely the open and lid-driven cavity configurations, with the primary goal of isolating issues related to pressure–velocity coupling. Here, we extend the same framework to a fully three-dimensional setting, thereby increasing both the physical complexity of the problem and the demands placed on the reduced-order model. This transition notably increases the physical realism and the computational demands placed upon the reduced system. Furthermore, our work addresses convection-dominated turbulent flows, a regime explicitly identified in the sources as being beyond the scope of the original study. Instead of relying solely on intrusive projection for all terms, we implement a hybrid data-driven methodology, where the turbulent closure is resolved non-intrusively, thereby bridging the gap between physical consistency and machine learning performance for complex 3D flows.

In this framework, LSTM, Transformer and MLP were investigated and compared in order to identify the most suitable model for accurately reproducing the temporal dynamics and nonlinear interactions of the turbulent flow.

The paper is structured as follows. Section 2 presents the methodology, starting from the mathematical formulation, detailing the FOM discretization, and describing the ROM approach. Section 3 reports the numerical results, including the selected test case, the flow behavior obtained with the proposed methodology, and a comparison of different neural network architectures to assess which performs best. Finally, Section 4 summarizes the main conclusions and outlines possible directions for future research.

## 2 Methodology

In this section, we will show the methodology used to obtain the results.

### 2.1 Mathematical model

In this study, the incompressible Navier–Stokes equations are adopted to describe the flow dynamics.

Let  $\Omega$  denote the computational domain corresponding to the fluid region. We consider an incompressible Newtonian fluid characterized by constant density  $\rho$  and kinematic viscosity  $\nu$ , in the absence of gravitational and body force effects. Under these assumptions, the governing equations consist of the conservation laws for mass and momentum.

$$\nabla \cdot \mathbf{u} = 0 \quad \text{in } \Omega, \quad (1)$$

$$\frac{\partial \mathbf{u}}{\partial t} = -\nabla \cdot (\mathbf{u} \otimes \mathbf{u}) + \nu \nabla \cdot (\nabla \mathbf{u}) - \nabla p \quad \text{in } \Omega, \quad (2)$$

Here,  $\mathbf{u}(\mathbf{x}, t)$  denotes the velocity field defined over the spatial domain  $\Omega \subset \mathbb{R}^d$ , with  $d = 2$  or  $3$ , while  $p(\mathbf{x}, t)$  is the pressure field normalized by the constant fluid density  $\rho$ . The time variable is indicated by  $t$ . The momentum equation accounts for convective transport, viscous diffusion, and pressure forces through the corresponding differential operators.

To account for the effects of turbulence within the FOM, a Large Eddy Simulation (LES) approach is adopted. In this framework, the governing equations are filtered at the grid scale, and the influence of the unresolved subgrid-scale (SGS) motions is modeled using the Smagorinsky subgrid-scale model.

Consequently, the molecular kinematic viscosity  $\nu$  in Equation 2 is replaced by an effective viscosity  $\nu_{eff}$ , defined as:

$$\nu_{eff} = \nu + \nu_T, \quad (3)$$

where  $\nu_T$  represents the turbulent eddy viscosity. In the context of the Smagorinsky model, this eddy viscosity is computed based on the resolved velocity field:

$$\nu_T = (C_s \Delta)^2 |\bar{S}|, \quad (4)$$

where  $C_s$  is the Smagorinsky constant, which is set to 0.2 in this work,  $\Delta$  is the filter width related to the grid size, and  $|\bar{S}| = \sqrt{2\bar{S}_{ij}\bar{S}_{ij}}$  is the magnitude of the resolved-scale strain rate tensor. Additionally, the turbulent Prandtl number  $Pr_t$  is set to 0.9. This formulation ensures that the FOM snapshots used for training accurately capture the energy dissipation and transient dynamics of the 3D lid-driven cavity before the data is passed to the reduced-order framework. This explicit mathematical treatment at the FOM level ensures that the high-fidelity snapshots of velocity, pressure, and viscosity  $(\mathbf{u}, p, \nu_T)$  contain the necessary physical information for the subsequent training of the data-driven closure.

The governing equations are augmented by the initial velocity field:

$$\mathbf{u}(\mathbf{x}, 0) = \mathbf{u}_0(\mathbf{x}) \quad \text{in } \Omega,$$

in which this condition is assumed to be divergence-free,  $\nabla \cdot \mathbf{u}_0 = 0$ .

To solve the problem above, we have to impose boundary conditions. We consider two different time-independent boundary conditions: wall, moving lid; so we have  $\partial\Omega = \Gamma_{wall} \cup \Gamma_{up}$ .

The no-slip condition is satisfied at the wall in case of viscous fluid, so we have to impose the following condition:

$$\mathbf{u} = \mathbf{u}_{wall}(\mathbf{x}) \quad \text{on } \Gamma_{wall} \quad \text{for } t \geq 0,$$

where  $\mathbf{u}_{wall}$  denotes the prescribed wall velocity. For stationary walls, this quantity is set equal to zero.

A moving lid condition is imposed on the upper boundary according to

$$\mathbf{u} = \mathbf{u}_{up}(\mathbf{x}) \quad \text{on } \Gamma_{up} \quad \text{for } t \geq 0,$$

where  $\mathbf{u}_{up}$  specifies the imposed tangential velocity of the lid, assumed to be uniform and known a priori.

For the pressure field, the boundary condition that we give is the zero-gradient condition on every wall. The turbulent viscosity has the condition of fixed value at every wall, it is zero.

## 2.2 FOM numerical discretization

This section describes the finite-volume discretization of the governing equations, Equations 1 and 2, formulated on a collocated grid arrangement (see Figure 1).

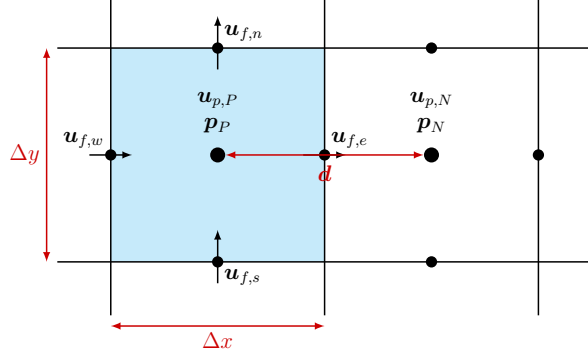


Figure 1: Two-dimensional collocated control-volume layout. Cell-centered velocity and pressure are associated with the control volumes  $P$  and  $N$ . Face fluxes  $\mathbf{u}_f$  are indicated on the cell faces, and  $\Delta x$ ,  $\Delta y$  denote the grid spacing. The vector  $\mathbf{d}$  connects adjacent cell centers.

To maintain local conservation of mass and momentum within the Finite Volume framework, the governing equations (Eqs. 1 and 2) are expressed in their integral form over each computational cell:

$$\int_{\partial(\Omega_h)_k} \mathbf{n} \cdot \mathbf{u} dS = 0, \quad (5)$$

$$\int_{(\Omega_h)_k} \frac{\partial \mathbf{u}}{\partial t} d\Omega = - \int_{\partial(\Omega_h)_k} (\mathbf{n} \cdot \mathbf{u}) \mathbf{u} dS + \nu \int_{\partial(\Omega_h)_k} \mathbf{n} \cdot (\nabla \mathbf{u}) dS - \int_{\partial(\Omega_h)_k} \mathbf{n} p dS, \quad (6)$$

Here,  $k$  denotes a generic control volume of the mesh, with  $(\Omega_h)_k$  indicating the associated cell volume and  $\partial(\Omega_h)_k$  its boundary surface. The integrals are evaluated over the cell interior and its boundary through the volume and surface measures  $d\Omega$  and  $dS$ , respectively.

For spatial discretization, we rewrite the governing equations (Equations 5 and 6) with matrix-vector notation:

$$\mathbf{M} \mathbf{u}_f = \mathbf{0}, \quad (7)$$

$$\frac{d\mathbf{u}_p}{dt} = -\mathbf{C}_p(\mathbf{u}_f, \mathbf{u}_p) - \mathbf{r}_p^C + \nu \mathbf{D}_p \mathbf{u}_p - \mathbf{G}_p \mathbf{p}_p + \nu \mathbf{r}_p^D, \quad (8)$$

Here,  $\mathbf{p}_p = (p_{p,1}, p_{p,2}, \dots, p_{p,h})^T \in \mathbb{R}^h$  denotes the pressure degrees of freedom associated with the cell centers, while  $\mathbf{u}_p \in \mathbb{R}^{dh}$  collects the corresponding cell-centered velocity components. In three spatial dimensions ( $d = 3$ ), the velocity vector is organized by grouping the Cartesian components, such that  $\mathbf{u}_p = ((\mathbf{u}_p)_1, (\mathbf{u}_p)_2, (\mathbf{u}_p)_3)^T$ , with each component containing the values defined over the  $h$  control volumes. The face-based velocity vector  $\mathbf{u}_f \in \mathbb{R}^{dm}$  is defined on the mesh faces and is obtained from the cell-centered velocity field through a linear interpolation operator  $\mathbf{I}_{p \rightarrow f}$ , together with prescribed boundary contributions, according to

$$\mathbf{u}_f = \mathbf{I}_{p \rightarrow f} \mathbf{u}_p + \mathbf{u}_b.$$

The vector  $\mathbf{u}_b \in \mathbb{R}^{dm}$  contains the velocity values imposed on the boundary faces of the computational domain.

The discrete operators appearing in the formulation are defined as follows. The matrix  $\mathbf{M} \in \mathbb{R}^{h \times dm}$  maps face-based quantities to cell centers and corresponds to the discrete divergence operator. Diffusive effects are accounted for through the cell-centered Laplacian operator  $\mathbf{D}_p \in \mathbb{R}^{dh \times dh}$ . Convective transport is described by the nonlinear operator  $\mathbf{C}_p(\mathbf{u}_f, \mathbf{u}_p) \in \mathbb{R}^{dh \times dh}$ , which depends on both face-centered and cell-centered velocity fields. The pressure gradient contribution is introduced via the

discrete gradient operator  $\mathbf{G}_p \in \mathbb{R}^{dh \times h}$ . In addition, the vectors  $\mathbf{r}_p^C \in \mathbb{R}^{dh}$  and  $\mathbf{r}_p^D \in \mathbb{R}^{dh}$  collect the convective and diffusive source terms, respectively.

The spatial discretization of the governing equations, written in integral form in Equations 5 and 6, is described below for a generic control volume  $k$ . The resulting discrete operators appearing in Equations 7 and 8 are detailed accordingly.

The continuity equation is discretized as following:

$$\int_{\partial(\Omega_h)_k} \mathbf{n} \cdot \mathbf{u} dS = \sum_{i=1}^{N_f} \int_{S_{f,i}} \mathbf{n} \cdot \mathbf{u} dS \approx \sum_{i=1}^{N_f} \mathbf{S}_{f,i} \cdot \mathbf{u}_{f,i} = \sum_{i=1}^{N_f} \phi_{f,i} = 0, \quad (9)$$

Here,  $N_f$  denotes the number of faces associated with control volume  $k$ , and  $S_f$  represents the area of a generic face. The discrete divergence operator  $\mathbf{M}$  introduced in Equation 7 is constructed from the outward-oriented face area vectors corresponding to the faces of the computational mesh. As expressed in Equation 9, the incompressibility condition is enforced at the level of the face fluxes, defined as  $\phi_f = \mathbf{S}_f \cdot \mathbf{u}_f$ .

For subsequent developments, it is also convenient to introduce a center-to-center divergence operator  $\mathbf{M}_p \in \mathbb{R}^{h \times dh}$ , obtained by composing the face-based operator with the interpolation from cell centers to faces, namely

$$\mathbf{M}_p = \mathbf{M} \mathbf{I}_{p \rightarrow f}.$$

Now we can write the momentum equation (Equation 8) as following:

$$\mathbf{M} \mathbf{u}_f = \mathbf{M} \mathbf{I}_{p \rightarrow f} \mathbf{u}_p + \mathbf{M} \mathbf{u}_b = \mathbf{M}_p \mathbf{u}_p + \mathbf{r}_p^M = \mathbf{0}, \quad (10)$$

The vector  $\mathbf{r}_p^M \in \mathbb{R}^h$  accounts for the boundary contributions associated with the continuity equation. It is defined through the action of the discrete divergence operator on the prescribed boundary velocity field,

$$\mathbf{r}_p^M = \mathbf{M} \mathbf{u}_b, \quad (11)$$

The pressure gradient contribution is obtained by applying the FV formulation to the pressure field over the boundary of a generic control volume. In particular, the surface integral is evaluated by summing the fluxes across the cell faces,

$$\int_{\partial(\Omega_h)_k} \mathbf{n} p dS = \sum_{i=1}^{N_f} \int_{S_{f,i}} \mathbf{n} p dS \approx \sum_{i=1}^{N_f} \mathbf{S}_{f,i} p_{f,i}.$$

Here,  $\mathbf{p}_f$  and  $\mathbf{p}_p$  denote the pressure values at face centers and cell centers, respectively. The two representations are related through a linear interpolation operator  $\mathbf{\Pi}_{p \rightarrow f} \in \mathbb{R}^{m \times h}$ , such that

$$\mathbf{p}_f = \mathbf{\Pi}_{p \rightarrow f} \mathbf{p}_p.$$

Within this formulation, the discrete pressure gradient operator  $\mathbf{G}_p$  is constructed from the face area vectors weighted by the interpolation coefficients contained in  $\mathbf{\Pi}_{p \rightarrow f}$ .

The diffusive term is discretized as following:

$$\int_{\partial(\Omega_h)_k} \mathbf{n} \cdot (\nabla \mathbf{u}) dS = \sum_{i=1}^{N_f} \int_{S_{f,i}} \mathbf{n} \cdot \nabla \mathbf{u} dS \approx \sum_{i=1}^{N_f} |\mathbf{S}_{f,i}| \frac{\mathbf{u}_{p,N} - \mathbf{u}_{p,P}}{|\mathbf{d}|},$$

where  $\mathbf{d}$  denotes the vector connecting the centers of the neighboring cells  $N$  and  $P$ .  $\mathbf{D}_p$  is the discrete operator of the discrete term, given by the areas of the faces and the distances between the two centers. In case one cell is near to another of the same domain, the discretization changes into:

$$|\mathbf{S}_{f,b}| \frac{\mathbf{u}_{f,b} - \mathbf{u}_{p,P}}{|\mathbf{d}_n|},$$

which can be decomposed into two contributions:

$$|\mathbf{S}_{f,b}| \frac{\mathbf{0} - \mathbf{u}_{p,P}}{|\mathbf{d}_n|} + |\mathbf{S}_{f,b}| \frac{\mathbf{u}_{f,b} - \mathbf{0}}{|\mathbf{d}_n|},$$

where the diffusion contribution is accounted for through the operator  $\mathbf{D}_p$ , while boundary-related effects are gathered in the vector  $\mathbf{r}_p^D$ . Here,  $\mathbf{u}_{f,b}$  denotes the velocity prescribed on boundary face  $b$ ,  $\mathbf{d}_n$  represents the vector connecting the boundary face to the corresponding cell center, and  $\mathbf{S}_{f,b}$  is the associated face area vector.

Finally, the convective term is discretized as following:

$$\int_{\partial(\Omega_h)_k} (\mathbf{n} \cdot \mathbf{u}) \mathbf{u} dS = \sum_{i=1}^{N_f} \int_{S_{f,i}} (\mathbf{n} \cdot \mathbf{u}) \mathbf{u} dS \approx \sum_{i=1}^{N_f} (\mathbf{S}_{f,i} \cdot \mathbf{u}_{f,i}) = \sum_{i=1}^{N_f} \phi_{f,i} \mathbf{u}_{f,i}.$$

The convective contribution is represented by the operator  $\mathbf{C}_p(\mathbf{u}_f, \mathbf{u}_p)$ , whose nonlinear dependence arises from the face fluxes  $\phi_f$ . When a control-volume face lies on the boundary of the computational domain, the contribution  $(\mathbf{S}_{f,b} \cdot \mathbf{u}_{f,b}) \mathbf{u}_{f,b}$  is incorporated into the boundary vector  $\mathbf{r}_p^C \in \mathbb{R}^{dh}$ .

In the present formulation, the discretized convection term exhibits a quadratic dependence on the velocity field. This follows from the fact that the face-centered velocity  $\mathbf{u}_f$  is obtained through linear interpolation of the cell-centered velocity  $\mathbf{u}_p$ . Under this assumption, the convective contribution can be expressed in operator form as the action of a velocity-dependent matrix on  $\mathbf{u}_p$ , namely

$$\tilde{\mathbf{C}}_p(\mathbf{u}_f) \mathbf{u}_p = \mathbf{C}_p(\mathbf{u}_f, \mathbf{u}_p). \quad (12)$$

Applying Equation 10 into Equation 7 and Equation 12 into Equation 11, we obtain the complete spatioally discretize system of equations:

$$\begin{aligned} \mathbf{M}_p \mathbf{u}_p + \mathbf{r}_p^M &= \mathbf{0}, \\ \frac{d\mathbf{u}_p}{dt} &= -\tilde{\mathbf{C}}_p(\mathbf{u}_f) \mathbf{u}_p + \nu \mathbf{D}_p \mathbf{u}_p - \mathbf{G}_p \mathbf{p}_p + \mathbf{r}_p, \end{aligned}$$

Here,  $\mathbf{r}_p \in \mathbb{R}^{dh}$  denotes the combined boundary contribution, defined as  $\mathbf{r}_p = -\mathbf{r}_p^C + \nu \mathbf{r}_p^D$ . All discrete operators are appropriately scaled according to the finite-volume measures.

In the framework of explicit projection methods, a well-documented difficulty is the emergence of spurious pressure oscillations, commonly referred to as the checkerboard problem. This phenomenon typically arises when collocated grids are employed in conjunction with central-difference discretizations of both the velocity divergence  $\nabla \cdot \mathbf{U}$  and the pressure gradient  $\nabla p$ .

The underlying cause of this instability is the decoupling between pressure and velocity at adjacent cell centers. Such a decoupling leads to a violation of the compatibility conditions between the discrete divergence and gradient operators, which in turn gives rise to an extended stencil in the Pressure Poisson Equation (PPE) [25, 71, 72, 73, 74, 75].

A common approach used in practice is Rhie–Chow interpolation. The idea is to correct the face-centered velocities so that they are compatible with the pressure gradient, which avoids the appearance of non-physical oscillations in the pressure field. This correction is part of the PISO (Pressure Implicit with Splitting of Operators) algorithm and is implemented in solvers such as OpenFOAM[74, 73, 48]. In contrast, for explicit projection methods on collocated grids combined with explicit time integration schemes, the application of Rhie–Chow interpolation may be circumvented. Two principal strategies are typically employed to treat the fluxes in this context: the inconsistent flux method and the consistent flux method[60].

Within the inconsistent flux method, the face velocity  $\mathbf{u}_f$  is reconstructed through linear interpolation from the cell-centered velocity  $\mathbf{u}_p$  together with the pressure field. Conversely, the consistent flux method introduces an auxiliary governing equation for the face-centered velocity  $\mathbf{u}_f$ , leading to a more robust and accurate formulation. Both approaches are generally implemented with explicit time integration schemes, such as the forward Euler method [76, 77, 78, 79, 47, 60].

The present study will concentrate on the consistent flux method.

### 2.2.1 Inconsistent and Consistent flux methods

As explained in [60], the projection method first evaluates an intermediate velocity  $\mathbf{u}_p^*$  field by neglecting the pressure gradient contribution in the momentum equations:

$$\frac{\mathbf{u}_p^* - \mathbf{u}_p^n}{\Delta t} = -\tilde{\mathbf{C}}_p(\mathbf{u}_f^n) \mathbf{u}_p^n + \nu \mathbf{D}_p \mathbf{u}_p^n + \mathbf{r}_p.$$

The intermediate velocity field  $\mathbf{u}_p^*$  is subsequently adjusted through the pressure contribution:

$$\mathbf{u}_p^{n+1} = \mathbf{u}_p^* - \Delta t \mathbf{G}_p \mathbf{p}_p^{n+1}.$$

To enforce the incompressibility constraint, the velocity field is expressed as:

$$\mathbf{M}_p \mathbf{u}_p^{n+1} + \mathbf{r}_p^M = (\mathbf{M}_p \mathbf{u}_p^* + \mathbf{r}_p^M) - \Delta t \mathbf{M}_p \mathbf{G}_p \mathbf{p}_p^{n+1} = \mathbf{0},$$

and considering:

$$\mathbf{L}_p \mathbf{p}_p^{n+1} = \frac{1}{\Delta t} (\mathbf{M}_p \mathbf{u}_p^* + \mathbf{r}_p^M), \quad (13)$$

here,  $\mathbf{L}_p = \mathbf{M}_p \mathbf{G}_p \in \mathbb{R}^{h \times h}$  denotes the discrete Laplacian operator obtained by mapping cell-centered pressure gradients to the cell faces. In this formulation, the resulting pressure field may lose coupling between neighboring control volumes, leading to the appearance of non-physical checkerboard modes. To address this issue, the pressure gradient is instead evaluated directly at the cell faces by introducing an alternative operator  $\mathbf{L}_f \in \mathbb{R}^{h \times h}$  in place of  $\mathbf{L}_p$  [80, 81].

We obtain:

$$\mathbf{L}_f \mathbf{p}_p^{n+1} = \frac{1}{\Delta t} (\mathbf{M}_p \mathbf{u}_p^n + \mathbf{r}_p^M) + \mathbf{M}_p (-\tilde{\mathbf{C}}_p(\mathbf{u}_f^n) \mathbf{u}_p^n + \nu \mathbf{D}_p \mathbf{u}_p^n + \mathbf{r}_p), \quad (14)$$

$$\mathbf{u}_p^{n+1} = \mathbf{u}_p^n + \Delta t (-\tilde{\mathbf{C}}_p(\mathbf{u}_f^n) \mathbf{u}_p^n + \nu \mathbf{D}_p \mathbf{u}_p^n + \mathbf{r}_p) - \Delta t \mathbf{G}_p \mathbf{p}_p^{n+1}. \quad (15)$$

In the inconsistent flux formulation, face-centered velocities  $\mathbf{u}_f$  are obtained by interpolating the cell-centered field through the operator  $\mathbf{I}_{p \rightarrow f}$ . In contrast, the consistent flux approach incorporates the pressure field resulting from the solution of the pressure Poisson equation (Equation 13) in order to adjust the face fluxes accordingly.

Firstly we apply the linear interpolation operator onto the Equation 14:

$$\mathbf{u}_f^{n+1} = \mathbf{I}_{p \rightarrow f} [\mathbf{u}_p^n + \Delta t (-\tilde{\mathbf{C}}_p(\mathbf{u}_f^n) \mathbf{u}_p^n + \nu \mathbf{D}_p \mathbf{u}_p^n + \mathbf{r}_p) - \Delta t \mathbf{G}_p \mathbf{p}_p^{n+1}]. \quad (16)$$

Rather than computing the pressure gradient at cell centers, it is evaluated directly on the cell faces using a discrete operator  $\mathbf{G}_f \in \mathbb{R}^{dm \times h}$ , yielding

$$\mathbf{u}_f^{n+1} = \mathbf{I}_{p \rightarrow f} [\mathbf{u}_p^n + \Delta t (-\tilde{\mathbf{C}}_p(\mathbf{u}_f^n) \mathbf{u}_p^n + \nu \mathbf{D}_p \mathbf{u}_p^n + \mathbf{r}_p)] - \Delta t \mathbf{G}_f \mathbf{p}_p^{n+1}, \quad (17)$$

for a generic cell  $k$ , the pressure gradient contribution appearing in the last term of Equation 17 is evaluated as

$$\sum_{i=1}^{N_f} \mathbf{S}_{f,i} \frac{p_{p,N} - p_{p,P}}{|\mathbf{d}|}.$$

The operator  $\mathbf{G}_f$  is constructed from coefficients involving the face-normal vectors and inverse center-to-center distances. In this formulation, pressure gradients are computed directly from cell-centered pressure values, whereas the operator  $\mathbf{G}_p$  relies on interpolated pressure fields evaluated at the cell centers.

By taking the divergence of Equation 16, according to Equation 10, we obtain:

$$\mathbf{M} \mathbf{u}_f^{n+1} = (\mathbf{M}_p \mathbf{u}_p^n + \mathbf{r}_p^M) + \mathbf{M}_p [\Delta t (-\tilde{\mathbf{C}}_p(\mathbf{u}_f^n) \mathbf{u}_p^n + \nu \mathbf{D}_p \mathbf{u}_p^n + \mathbf{r}_p)] - \Delta t \mathbf{M} \mathbf{G}_f \mathbf{p}_p^{n+1}. \quad (18)$$

So, substituting the pressure, we can see that the  $\mathbf{u}_f$  is divergence free.

Finally, the system of equations for the CFM is formed by Equations 14, 15 and 17, which are solved in this particular order to obtain  $\mathbf{u}_f$ ,  $\mathbf{u}_p$  and  $\mathbf{p}_p$  at time  $t^{n+1}$ .

## 2.3 ROM approach

ROM in this study is constructed through a hybrid strategy designed to handle the complexities of turbulent flows. As established in previous studies [60], the standard 'discretize-then-project' approach provides high accuracy for laminar regimes but encounters a significant physical inconsistency when applied to turbulent viscosity field  $\nu_T$ .

Specifically, while the intrusive Galerkin projection accurately resolves the temporal coefficients for velocity  $\mathbf{u}$  and pressure  $p$ , it fails to yield a physically coherent representation of the turbulent viscosity in the reduced space. To address this, we adopt a dual-path framework:

- **Intrusive Path:** The fields of pressure and velocity are resolved via the consistent flux discretize-then-project methodology to ensure mass conservation.
- **Non-Intrusive Path:** The turbulent viscosity field, originally modeled in the FOM using the Smagorinsky LES framework, is reconstructed using a data-driven closure (specifically an LSTM network).

This hybrid formulation enables the efficient simulation of unsteady turbulent flows by combining the mathematical rigor of projection-based ROMs with the predictive adaptability of deep learning.

### 2.3.1 POD-GALERKIN Method

The consistent flux formulation is projected onto a reduced space by applying the POD–Galerkin procedure to the fully discrete equations given in Equations 14, 15 and 17. This formulation relies on the assumption that the full-order solution admits a reduced representation in terms of orthonormal spatial basis functions with coefficients that vary in time.

These modes,  $\Phi$  (cell-centered velocity),  $\mathbf{X}$  (cell-centered pressure), and  $\Psi$  (face velocity), are defined as global because they are computed across the entire discrete spatial domain  $\Omega_h$  or the total set of face areas  $\Sigma$ . Unlike local nodal values, these basis functions capture the dominant energy-containing coherent structures of the flow during high-fidelity simulations. The  $\mathbf{u}_p$  as discrete cell-centered velocity fields can be approximated by:

$$\mathbf{u}_p \approx \mathbf{u}_{p,r} = \Phi \mathbf{a}, \quad (19)$$

where  $\Phi = (\phi_1, \dots, \phi_{N_r^u}) \in \mathbb{R}^{dh \times N_r^u}$  contains the global velocity modes  $\phi_i \in \mathbb{R}^{dh}$  and  $\mathbf{a} = (a^1, \dots, a^{N_r^u}) \in \mathbb{R}^{N_r^u}$  are the temporal coefficients with  $N_r^u$  the number of velocity modes. Similar approximations are used for the pressure field  $\mathbf{p}_p$  and the face velocity field  $\mathbf{u}_f$ .

The pressure field in discrete form is represented as

$$\mathbf{p}_p \approx \mathbf{p}_{p,r} = \mathbf{X} \mathbf{b}, \quad (20)$$

here,  $\mathbf{X} = (\chi_1, \dots, \chi_{N_r^p}) \in \mathbb{R}^{h \times N_r^p}$  collects the pressure basis functions defined at the cell centers, with each mode  $\chi = (\chi_1, \dots, \chi_h)^T \in \mathbb{R}^h$ . The vector  $\mathbf{b}^n = (b^1, \dots, b^{N_r^p}) \in \mathbb{R}^{N_r^p}$  are the corresponding time-dependent coefficients with  $N_r^p$  the number of pressure modes.

Within the reduced-order framework, the face velocity field is expressed as

$$\mathbf{u}_f \approx \mathbf{u}_{f,r} = \Psi \mathbf{c}, \quad (21)$$

where  $\Psi = (\psi_1, \dots, \psi_{N_r^u}) \in \mathbb{R}^{dm \times N_r^u}$  is a matrix containing the face velocity modes  $\psi_i \in \mathbb{R}^m$  and  $\mathbf{c}(t) = (c^1, \dots, c^{N_r^u}) \in \mathbb{R}^{N_r^u}$  are the the associated time-varying coefficients.

The computation of these global modes follows the Method of Snapshots. Taking the velocity field as a representative example, the procedure involves:

1. **Snapshot Collection:** A set of  $N_s^u$  high-fidelity solutions is collected:  $\mathcal{S} = \{\mathbf{u}_p^1, \dots, \mathbf{u}_p^{N_s^u}\}$ .
2. **Correlation Matrix Construction:** A matrix  $\mathbf{C}^u \in \mathbb{R}^{N_s^u \times N_s^u}$  is computed using the discrete  $L_2$ -inner product over the entire domain:

$$C_{i,j}^u = (\mathbf{u}_p^i, \mathbf{u}_p^j)_{L_2(\Omega_h)} = \sum_{k=1}^h \mathbf{u}_{p,k}^i \cdot \mathbf{u}_{p,k}^j (\Omega_h)_k,$$

where  $(\Omega_h)_k$  is the volume of the  $k$ -th mesh cell.

3. **Eigenvalue Problem Resolution:** We solve  $\mathbf{C}^u \mathbf{Q}^u = \mathbf{Q}^u \lambda^u$  to determine the eigenvectors  $\mathbf{Q}^u$  and eigenvalues  $\lambda^u$ .
4. **Global Mode Reconstruction:** The modes  $\phi_i$  are constructed as an orthonormal linear combination of the snapshots:

$$\phi_i = \frac{1}{N_s^u \sqrt{\lambda_{ii}^u}} \sum_{n=1}^{N_s^u} \mathbf{u}_p^n Q_{in}^u \quad \text{for } i = 1, \dots, N_r^u.$$

The cell-centered velocity modes  $\phi$  are only approximately divergence-free, matching the behaviour of the cell-centered velocity field  $\mathbf{u}_p$ . Consequently, the pressure contribution must be retained in the reduced-order formulation.

We now derive the Galerkin projection corresponding to the consistent flux method. To this end, the approximations of the cell-centered velocity  $\mathbf{u}_p$ , the cell-centered pressure  $\mathbf{p}_p$ , and the face velocity  $\mathbf{u}_f$  (Equations 19, 20, and 21) are substituted into Equations 14, 15 and 17. The Pressure Poisson Equation (PPE) is subsequently formulated in the reduced pressure space by left-multiplying both sides of the equation by  $\mathbf{X}^T \mathbf{V}$ :

$$\mathbf{X}^T \mathbf{V} \mathbf{L}_f \mathbf{X} \mathbf{b}^{n+1} = \frac{1}{\Delta t} (\mathbf{X}^T \mathbf{V} \mathbf{M}_p \phi \mathbf{a}^n + \mathbf{X}^T \mathbf{V} \mathbf{r}_p^M) + \mathbf{X}^T \mathbf{V} \mathbf{M}_p (-\tilde{\mathbf{C}}_p (\mathbf{I}_{p \rightarrow f} \phi \mathbf{a}^n) \phi \mathbf{a}^n + \nu \mathbf{D}_p \phi \mathbf{a}^n + \mathbf{r}_p).$$

where  $\mathbf{V} \in \mathbb{R}^{h \times h}$  is a diagonal matrix collecting the cell-centered control-volume measures.

We can rewrite this equation as follows:

$$\mathbf{L}_r \mathbf{b}^{n+1} = \frac{1}{\Delta t} (\mathbf{M}_r \mathbf{a}^n + \mathbf{q}_r^M) - \hat{\mathbf{A}}_r (\mathbf{a}^n) \mathbf{a}^n + \nu \mathbf{B}_r \mathbf{a}^n + \mathbf{q}_r,$$

where

- $\mathbf{L}_r = \mathbf{X}^T \mathbf{V} \mathbf{L}_f \mathbf{X} \in \mathbb{R}^{N_r^p \times N_r^p}$ ,
- $\mathbf{M}_r = \mathbf{X}^T \mathbf{V} \mathbf{M}_p \Phi \in \mathbb{R}^{N_r^p \times N_r^u}$ ,
- $\mathbf{B}_r = \mathbf{X}^T \mathbf{V} \mathbf{M}_p \mathbf{D}_p \Phi \in \mathbb{R}^{N_r^p \times N_r^u}$ ,
- $\mathbf{q}_r = \mathbf{X}^T \mathbf{V} \mathbf{M}_p \mathbf{r}_p \in \mathbb{R}^{N_r^p}$ ,
- $\hat{\mathbf{A}}_r = \mathbf{X}^T \mathbf{V} \mathbf{M}_p \tilde{\mathbf{C}}_p (\mathbf{I}_{p \rightarrow f} \Phi) \Phi \in \mathbb{R}^{N_r^p \times N_r^u N_r^p \times N_r^u}$ .

The first three are linear terms, the fourth is a reduced vector and the fifth term is the non-linear convection term; they are all determined during the offline stage. Therefore,  $\hat{\mathbf{A}}_r (\mathbf{a}^n) \mathbf{a}^n$  during the online stage is evaluated as:

$$\sum_{i=1}^{N_r^u} (\mathbf{a}^n)^T \hat{\mathbf{A}}_{r,i} \mathbf{a}^n.$$

The discretized momentum Equation 15 is projected onto the reduced base obtained from the velocity modes, multiplying the left hand of the equation for  $\Phi^T \mathbf{V}$ :

$$\Phi^T \mathbf{V} \Phi \mathbf{a}^{n+1} = \Phi^T \mathbf{V} \Phi \mathbf{a}^n + \Delta t \phi^T \mathbf{V} (-\tilde{\mathbf{C}}_p (\mathbf{I}_{p \rightarrow f} \Phi \mathbf{a}^n) \Phi \mathbf{a}^n + \nu \mathbf{D}_p \Phi \mathbf{a}^n + \mathbf{r}_p) - \Delta t \Phi^T \mathbf{V} \mathbf{G}_p \mathbf{X} \mathbf{b}^{n+1}.$$

We can rewrite it as follows:

$$\mathbf{a}^{n+1} = \mathbf{a}^n + \Delta t (-\hat{\mathbf{C}}_r (\mathbf{a}^n) \mathbf{a}^n + \nu \mathbf{D}_r \mathbf{a}^n + \mathbf{r}_r) - \Delta t \hat{\mathbf{G}}_r \mathbf{b}^{n+1},$$

with

- $\mathbf{D}_r = \Phi^T \mathbf{V} \mathbf{D}_p \Phi \in \mathbb{R}^{N_r^u \times N_r^u}$ ,
- $\hat{\mathbf{G}}_r = \Phi^T \mathbf{V} \mathbf{G}_p \mathbf{X} \in \mathbb{R}^{N_r^u \times N_r^p}$ ,
- $\mathbf{r}_r = \Phi^T \mathbf{V} \mathbf{r}_p \Phi \in \mathbb{R}^{N_r^u}$ ,
- $\hat{\mathbf{C}}_r (\mathbf{a}^n) \in \mathbb{R}^{N_r^u \times N_r^u \times N_r^u}$ .

The first two are reduced matrices, the third is a reduced vector and the fourth is a tensor; they are all determined during the offline stage.

To derive the governing system associated with the consistent flux formulation, the reduced representations of the cell-centered velocity, face-centered velocity, and pressure fields Equations 19, 20, and 21 are inserted into the corresponding full-order discrete Equations 14, 15, and 17, yielding:

$$\mathbf{L}_r \mathbf{b}^{n+1} = \frac{1}{\Delta t} (\mathbf{M}_r \mathbf{a}^n + \mathbf{q}_r^M) - \mathbf{A}_r(\mathbf{c}^n) \mathbf{a}^n + \nu \mathbf{B}_r \mathbf{a}^n + \mathbf{q}_r, \quad (22)$$

$$\mathbf{a}^{n+1} = \mathbf{a}^n + \Delta t (-\mathbf{C}_r(\mathbf{c}^n) \mathbf{a}^n + \nu \mathbf{d}_r \mathbf{a}^n + \mathbf{r}_r) - \Delta t \hat{\mathbf{G}}_r \mathbf{b}^{n+1}, \quad (23)$$

$$\mathbf{W}_r \mathbf{c}^{n+1} = \mathbf{N}_r \mathbf{a}^n + \Delta t (-\mathbf{K}_r(\mathbf{c}^n) \mathbf{a}^n + \nu \mathbf{P}_r \mathbf{a}^n + \mathbf{s}_r) - \Delta t \mathbf{G}_r \mathbf{b}^{n+1}, \quad (24)$$

with

- $\mathbf{W}_r = \Psi^T \Sigma \Psi \in \mathbb{R}^{N_r^u \times N_r^u}$ ,
- $\mathbf{N}_r = \Psi^T \Sigma \mathbf{I}_{p \rightarrow f} \Phi \in \mathbb{R}^{N_r^u \times N_r^u}$ ,
- $\mathbf{P}_r = \Psi^T \Sigma \mathbf{D}_p \Phi \in \mathbb{R}^{N_r^u \times N_r^u}$ ,
- $\mathbf{G}_r = \Psi^T \Sigma \mathbf{G}_f \mathbf{X} \in \mathbb{R}^{N_r^u \times N_r^p}$ ,
- $\mathbf{s}_r = \Psi^T \Sigma \mathbf{r}_p \in \mathbb{R}^{N_r^u}$ .

where  $\Sigma \in \mathbb{R}^{dm \times dm}$  is the matrix that stores the face-area information associated with the computational cells.

The last one is the reduced vector and the other are matrices. The reduced convection terms  $\mathbf{A}_r(\mathbf{a}^n) \in \mathbb{R}^{N_r^u \times N_r^u \times N_r^u}$ ,  $\mathbf{C}_r(\mathbf{a}^n) \in \mathbb{R}^{N_r^u \times N_r^u \times N_r^u}$  and  $\mathbf{K}_r(\mathbf{a}^n) \in \mathbb{R}^{N_r^u \times N_r^u \times N_r^u}$  are determined, respectively, by

$$\begin{aligned} \mathbf{A}_{r,i} &= \mathbf{X}^T \mathbf{V} \mathbf{M}_p \tilde{\mathbf{C}}_p(\Psi_i) \Phi, \\ \mathbf{C}_{r,i} &= \Phi^T \mathbf{V} \tilde{\mathbf{C}}_p(\Psi_i) \Phi, \\ \mathbf{K}_{r,i} &= \Psi^T \Sigma \tilde{\mathbf{C}}_p(\Psi_i) \Phi. \end{aligned}$$

In this way, we obtain POD modes that are divergence free, because the divergence-free condition is satisfied at the discrete level by the face-centered velocity fields.

## 2.4 Closure Model

In recent years, the evolution of machine learning techniques has increasingly highlighted the role of data-driven methods. This term refers to approaches in which decisions, predictions, and analyses are not guided by predefined theoretical models or manually designed rules, but instead emerge directly from the available data. In other words, rather than describing in advance how a system should behave, the machine is allowed to “learn” from past observations, discovering patterns and regularities that can be used to tackle new cases. This shift in perspective has revolutionized fields ranging from medicine to finance, from robotics to natural language processing.

Data-driven approaches rely on the availability of data rather than on explicitly prescribed physical models. In practice, this often leads to the use of artificial neural networks, which are able to approximate complex input–output relationships when sufficient data are available. Over the years, a variety of network architectures have been proposed, and their suitability depends strongly on the structure of the problem under consideration. In the present work, attention is restricted to three commonly used architectures, namely MLPs, LSTMs, and Transformer-based models.

An MLP is used as a simple neural baseline. The model is implemented as a sequence of fully connected layers with nonlinear activations and is trained to directly relate the reduced input variables to the target quantities. This architecture is known to work reasonably well for static regression problems. However, since no explicit mechanism is included to represent temporal structure, its effectiveness decreases when the solution depends strongly on the system dynamics over time, as is the case for unsteady flow fields.

To model the temporal evolution of the turbulent viscosity coefficients, recurrent neural network architectures are a natural choice, as the reduced-order dynamics exhibit strong temporal correlations. Among these architectures, LSTM networks are particularly suitable due to their ability to propagate information over extended time horizons in a stable manner. This property is essential in the present context, where the turbulent closure depends not only on the instantaneous reduced state but also on its recent temporal history. Compared to simpler feedforward models, the LSTM formulation provides

improved robustness when learning long-term dependencies, which is a known limitation of standard recurrent networks.

Transformer architectures are also considered in this work as a possible alternative for learning temporal dependencies in the reduced-order setting. Their attention-based formulation allows interactions between distant time instants to be represented without relying on recurrence, which can be beneficial when long-range correlations are present in the reduced dynamics. At the same time, this design leads to highly parallel training procedures, although its effectiveness in the present turbulent viscosity prediction task is not guaranteed a priori. For this reason, Transformers are included in the comparative analysis alongside recurrent and feedforward models.

#### 2.4.1 Neural Networks

In this work, as previously discussed, a data-driven strategy is employed to address the physical inconsistency encountered when applying standard projection techniques to the turbulent flows. While the 'discretize-then-project' methodology ensures consistency for velocity and pressure, it has been observed that standard Galerkin projection fails to yield a physically coherent representation of the turbulent viscosity field in the reduced space. This occurs because the intrusive projection is unable to accurately resolve the complex temporal evolution and non-linear interactions of the eddy viscosity within the reduced basis. To overcome this limitation, we adopt a hybrid approach: velocity and pressure are resolved via intrusive projection, while a LSTM neural network is used as a non-intrusive closure to predict the turbulent viscosity coefficients. The network is trained using the temporal coefficients of velocity  $u$  and pressure  $p$  obtained from high-fidelity FOM simulations.

Following the same logic, we also evaluated two other architectures, MLP and Transformer, to provide a comprehensive comparison. However, the LSTM demonstrated superior performance due to its inherent ability to capture the long-term temporal dependencies critical for unsteady turbulent phenomena; these results are detailed in the following chapter. All hyperparameters and architectural details for these three networks are reported in the section 4, see [Table 3](#) and [Table 2](#).

#### 2.4.2 Data driven method for turbulent viscosity prediction

The proposed data-driven closure in this study is specifically designed for eddy viscosity-based turbulence models, such as the Smagorinsky LES model employed in our numerical benchmarks. This approach is predicated on the Boussinesq hypothesis, which assumes that the influence of turbulent fluctuations can be effectively represented by an eddy (turbulent) viscosity  $\nu_T$  that modifies the transport properties of the fluid.

Using the FOM, we obtain the three primary fields of interest: velocity  $\mathbf{u}$ , pressure  $p$ , and turbulent viscosity  $\nu_T$ . To resolve these fields at the discrete level, we employ the CFM. The numerical procedure is defined as follows:

First, we define a forcing term,  $F_{aux}$ , which represents the variation in the velocity field due to convective and diffusive effects over a time step  $\Delta t$ :

$$F_{aux} = \Delta t[-\nabla \cdot (\phi \mathbf{U}) + \nabla \cdot (\nu_{eff} \nabla \mathbf{U})];$$

where  $-\nabla \cdot (\phi \mathbf{U})$  represents the nonlinear convective transport and  $\nabla \cdot (\nu_{eff} \nabla \mathbf{U})$  denotes the viscous diffusive term. In this formulation,  $\nu_{eff} = \nu + \nu_T$  is the effective viscosity, which combines the molecular kinematic viscosity  $\nu$  and the turbulent eddy viscosity  $\nu_T$ .

In the present formulation, the turbulent viscosity is explicitly retained in the diffusive term of the momentum equation. This differs from earlier discretize-then-project approaches developed for laminar flows, such as the framework presented in [\[60\]](#), where the turbulent contribution was not incorporated at the projection level. As a result, the present approach provides a more consistent treatment of diffusive effects when turbulent dynamics are considered.

The velocity field is then updated to obtain an intermediate state,  $\mathbf{U}_{aux}^{(1)}$ , which accounts for forcing but has not yet been corrected for pressure effects:

$$\mathbf{U}_{aux}^{(1)} = \mathbf{U} + F_{aux};$$

Subsequently, a Pressure Poisson Equation (PPE) is solved to enforce the incompressibility constraint:

$$\nabla^2 p = \frac{1}{\Delta t} \nabla \cdot U_{aux}^{(1)};$$

$$p(cellRef) = p_{ref};$$

Once the pressure field is obtained, the final velocity is corrected:

$$U = U_{aux}^{(1)} - \Delta t \nabla p;$$

This correction step enforces the incompressibility constraint by removing the divergence of the velocity field, while retaining the contribution of the turbulent eddy viscosity provided by the data-driven model.

The overall procedure adopted to predict the turbulent viscosity coefficients follows a sequential workflow that combines the consistent flux method with a non-intrusive neural-network-based closure. The main steps of the implementation are summarized below.

1. **Forcing Field Computation:** Calculate the forcing term  $F_{aux}$  by evaluating convective and diffusive transport, explicitly incorporating the effective viscosity  $\nu_{eff} = \nu + \nu_T$  to account for turbulent stresses.
2. **Intermediate Velocity Prediction:** Update the current velocity field to a provisional state  $U_{aux}^{(1)}$  by applying the forcing term, initially neglecting pressure contributions.
3. **Pressure Poisson Resolution:** Solve the Poisson equation for the normalized scalar pressure field  $p$  to enforce the incompressibility constraint.
4. **Velocity and Flux Correction:** Apply the computed pressure gradient  $\nabla p$  to correct the intermediate velocity field, ensuring a strictly divergence-free solution.
5. **Modal Coefficient Extraction:** Utilize the `ITHACUtilities::getCoeffs` function to extract the temporal modal coefficients for velocity, pressure, and turbulent viscosity from the snapshot dataset. These coefficients are essential for the training and validation of the NN developed to predict the turbulent viscosity field.
6. **Data Preprocessing and Normalization:** Normalize the extracted coefficients using a `StandardScaler` to improve convergence, while generating input sequences (velocity and pressure) and target sequences (turbulent viscosity), and the scaler is stored to enable denormalization after prediction.
7. **Neural Network Training (Offline Phase):** Execute the `model.fit` function to train the NN architecture like NN, enabling it to learn the non-linear temporal mappings between the reduced state and the eddy viscosity.
8. **Prediction and Reconstruction (Online Phase):** Deploy the trained model via `model.predict` and perform an inverse transform to reconstruct the physical turbulent viscosity field in the reduced space.

This procedure integrates the consistent flux formulation used for velocity and pressure with a non-intrusive, data-driven treatment of the turbulent closure. A schematic overview of the workflow is provided in Figure 2.

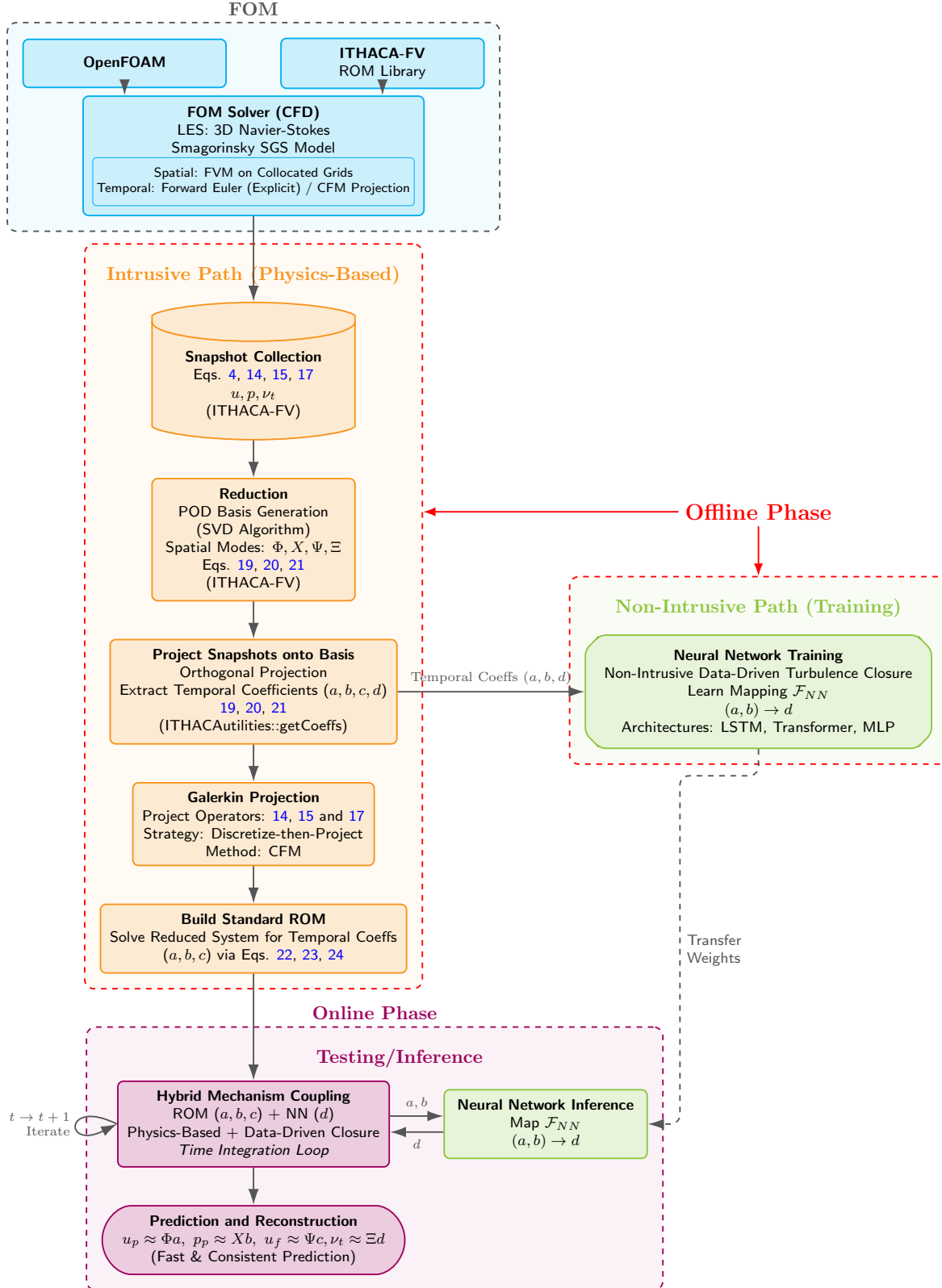


Figure 2: Detailed workflow of the proposed hybrid methodology combining a physics-based "discretize-then-project" ROM with a data-driven turbulence closure which is trained offline but integrated directly into the online time-stepping loop.

### 3 Numerical Results

#### 3.1 Test case description

This section outlines the numerical setup adopted in the present study. The benchmark problem considered is the classical lid-driven cavity, modeled in a three-dimensional domain. The simulations are performed using the consistent flux method, already available in ITHACA-FV, an open-source  $C^+$  library built on top of OpenFOAM. All numerical solvers rely on the OpenFOAM framework. The objective is to analyze the turbulent regime of this configuration, focusing on the reconstruction of velocity and pressure fields through ROM techniques, while turbulent viscosity is recovered via a data-driven approach.

The computational domain corresponds to a unit cube with edge length equal to 1 m. A structured mesh of  $50 \times 50 \times 50$  hexahedral cells is employed (Figure 3). On the top boundary, a uniform tangential velocity  $U = (1, 0, 0)$  m/s is prescribed, whereas no-slip boundary conditions are imposed on the remaining walls. Turbulence is modeled through a turbulent viscosity  $\nu_T$ , using a LES simulation with the Smagorinsky turbulence model: a uniform zero condition is enforced at the walls, and a zero-gradient condition is prescribed for pressure. In particular, the Smagorinsky constant is  $C_s = 0.2$  and the turbulent Prandtl number is  $Pr_t = 0.9$ .

The simulation is advanced for  $\Delta t = 2000$  time steps. The discretization schemes are chosen as follows: Euler forward for the temporal derivative, Gauss linear for gradients, Gauss linearUpwind for the divergence and Gauss linear orthogonal for the Laplacian. In the reduced-order framework, 10 POD modes are retained for each variable, namely velocity, pressure, and turbulent viscosity.



Figure 3: Computational domain and grid generation. The geometry of the cubic cavity is shown on the left, and the corresponding computational mesh is shown on the right

#### 3.2 Results

In the first stage, the FOM was solved in order to generate the high-fidelity data required for the subsequent offline phase of the ROM process. Following the discretize-then-project approach, POD was applied to the FOM solutions to extract the dominant spatial modes associated with velocity, pressure, and turbulent viscosity fields. The corresponding temporal coefficients were also computed, representing the time evolution of each mode. Together, these components form the basis of the ROM, which provides a compact yet accurate representation of the original high-dimensional system. In the subsequent online phase, the velocity and pressure fields were reconstructed from the ROM.

Based on the reduced-order results, the selected neural network (the LSTM model introduced earlier) was trained and validated using the data obtained from the ROM simulations. Specifically, the first 1800 snapshots were employed for training, while the remaining 200 snapshots were reserved for validation. The objective was to establish a data-driven strategy for predicting the turbulent viscosity field  $\nu_T$ , thereby enabling the resolution of turbulent flow problems through the hybrid ROM–data-driven framework described before (ROM technique for velocity and pressure and data-driven method for turbulent viscosity).

### 3.2.1 Visualization, plots and errors

To quantitatively validate the proposed approach, the obtained results are here presented and discussed. As a first step, the error between the FOM and the ROM was evaluated for different numbers of POD modes, with the aim of identifying the optimal number of modes to be used for this specific case study.

From this analysis (see 4), it can be observed that 10 represents the optimal number of POD modes, providing a good balance between accuracy and model reduction.

$$\frac{\int_0^T \int_{\Omega} (F_{\text{FOM}} - F_{\text{ROM}}) dx dt}{\int_0^T \int_{\Omega} F_{\text{FOM}} dx dt} \quad (25)$$

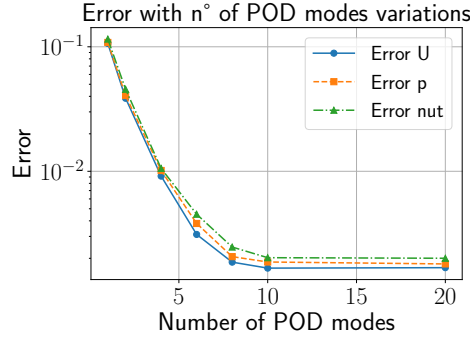


Figure 4: Plot of the error with modes variation, between the FOM solution and the ROM solution.

In Figure 5, 6 and 7 we show the plots of the errors between FOM and ROM problems with time variances:

$$\frac{\int_{\Omega} (F_{\text{FOM}} - F_{\text{ROM}}) dx}{\int_{\Omega} F_{\text{FOM}} dx} \quad (26)$$

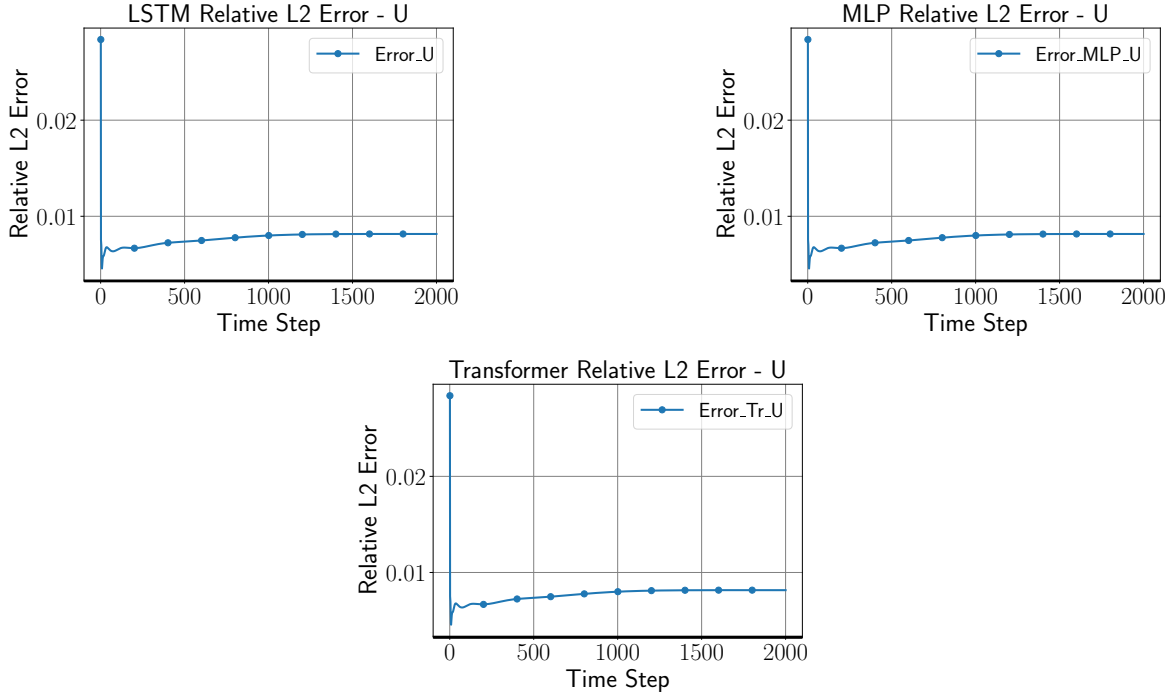


Figure 5: Plots of the errors, with time variation, for the velocity field between the FOM solution and the ROM solution with the three different neural networks used: on the left LSTM, in the center MLP, on the right Transformer.

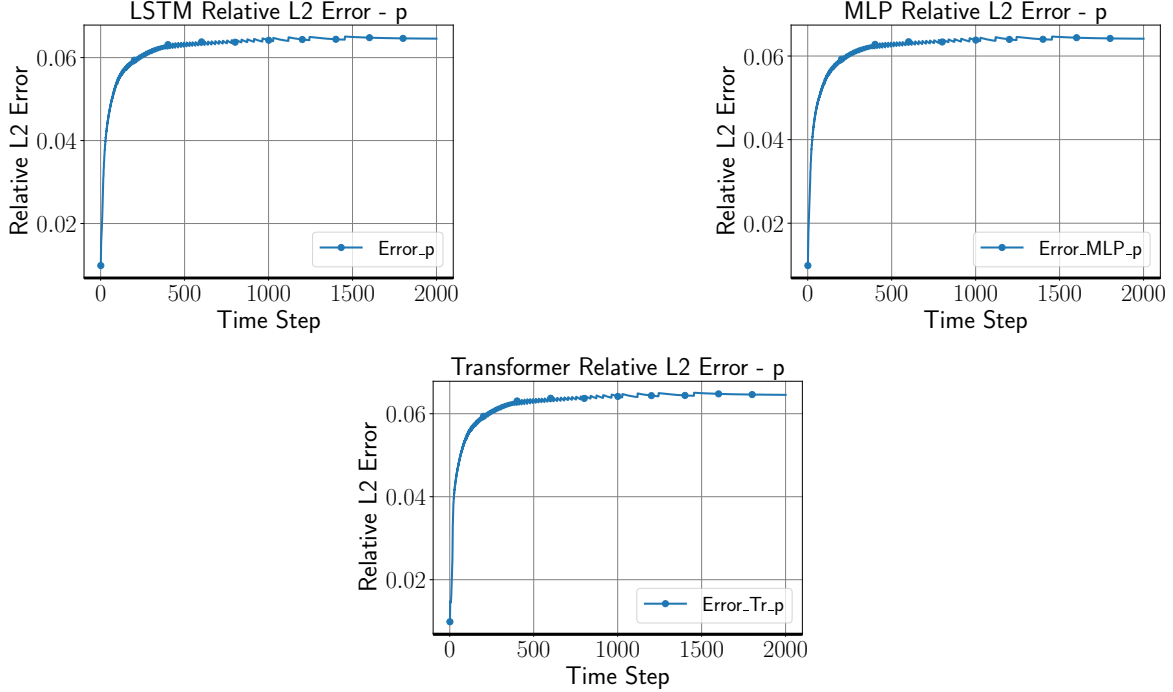


Figure 6: Plots of the errors, with time variation, for the pressure field between the FOM solution and the ROM solution with the three different neural networks used: on the left LSTM, in the center MLP, on the right Transformer.

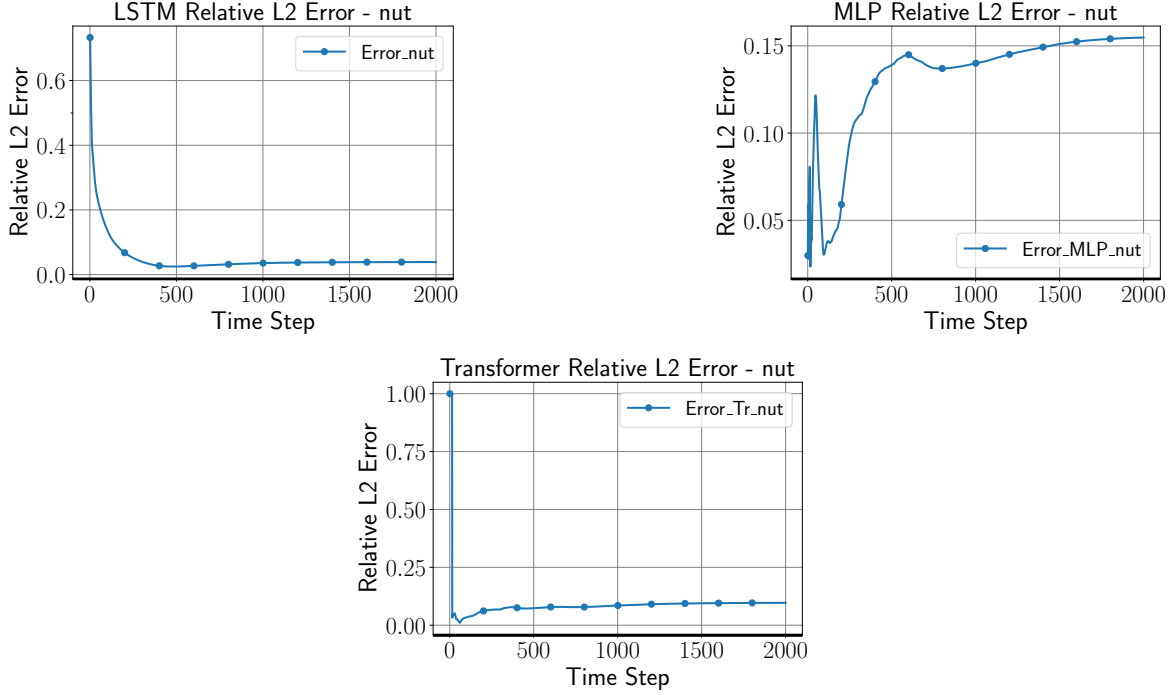


Figure 7: Plots of the errors, with time variation, for the turbulent viscosity field between the FOM solution and the ROM solution with the three different neural networks used: on the left LSTM, in the center MLP, on the right Transformer.

The error plots confirm that the LSTM neural network outperforms the other two architectures.

To complete the illustration of the results that we obtained, in Figure 8, 9 and 10 we show the comparison between the results of the FOM problem with respect to the ROM problem (LSTM case):

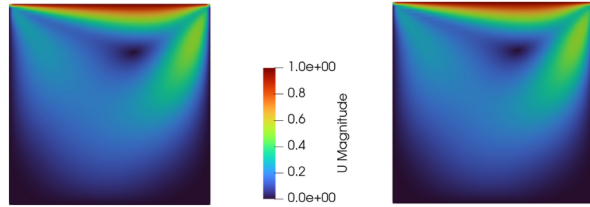


Figure 8: Velocity field on the section of the test case: on the left the FOM solution and on the right the ROM solution.

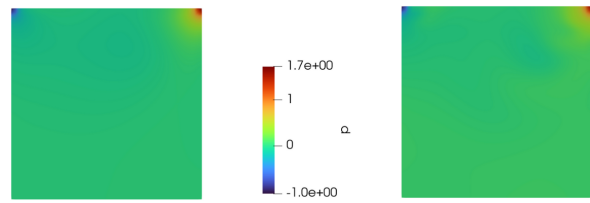


Figure 9: Pressure field on the section of the test case: on the left the FOM solution and on the right the ROM solution.

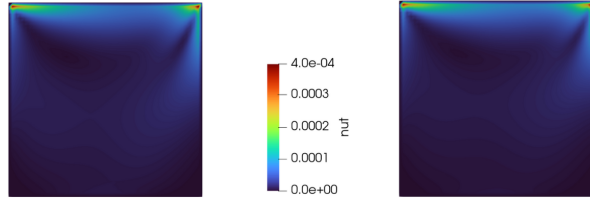


Figure 10: Turbulent viscosity field on the section of the test case: on the left the FOM solution and on the right the ROM solution.

We can see that the two results are barely the same; therefore, the approximation obtained with this hybrid technique, ROM + data-driven, is accurate for this kind of application.

In Figure 11, 12 and 13 we show the comparison between the different neural networks used: LSTM, MLP and Transformer.

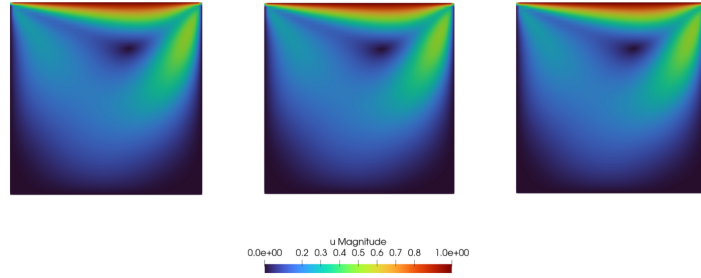


Figure 11: Velocity field on the section of the test case: on the left the the LSTM neural network solution; in the center the MLP neural network solution; on the right the Transformer neural network solution.

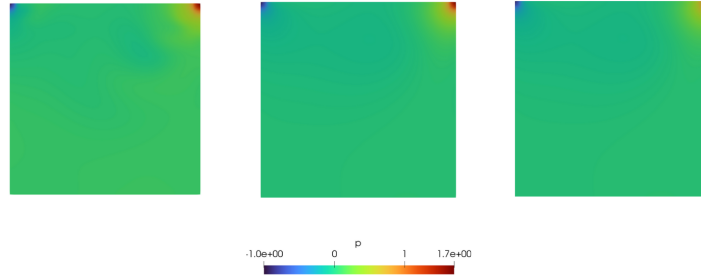


Figure 12: Pressure field on the section of the test case: on the left the the LSTM neural network solution; in the center the MLP neural network solution; on the right the Transformer neural network solution.

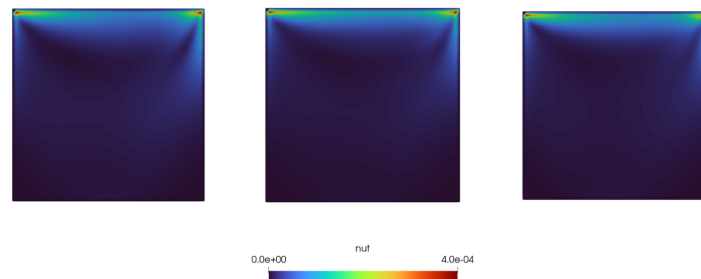


Figure 13: Turbulent viscosity field on the section of the test case: on the left the the LSTM neural network solution; in the center the MLP neural network solution; on the right the Transformer neural network solution.

Finally, to complete the analysis, we report in Figure 14 the errors in terms of energy and in Figure

15 the errors in term of entropy obtained for all architectures at number of POD modes fixed (10 POD modes). The entropy, in particular, is calculated to know how well a ROM model retains relevant information compared to FOM.

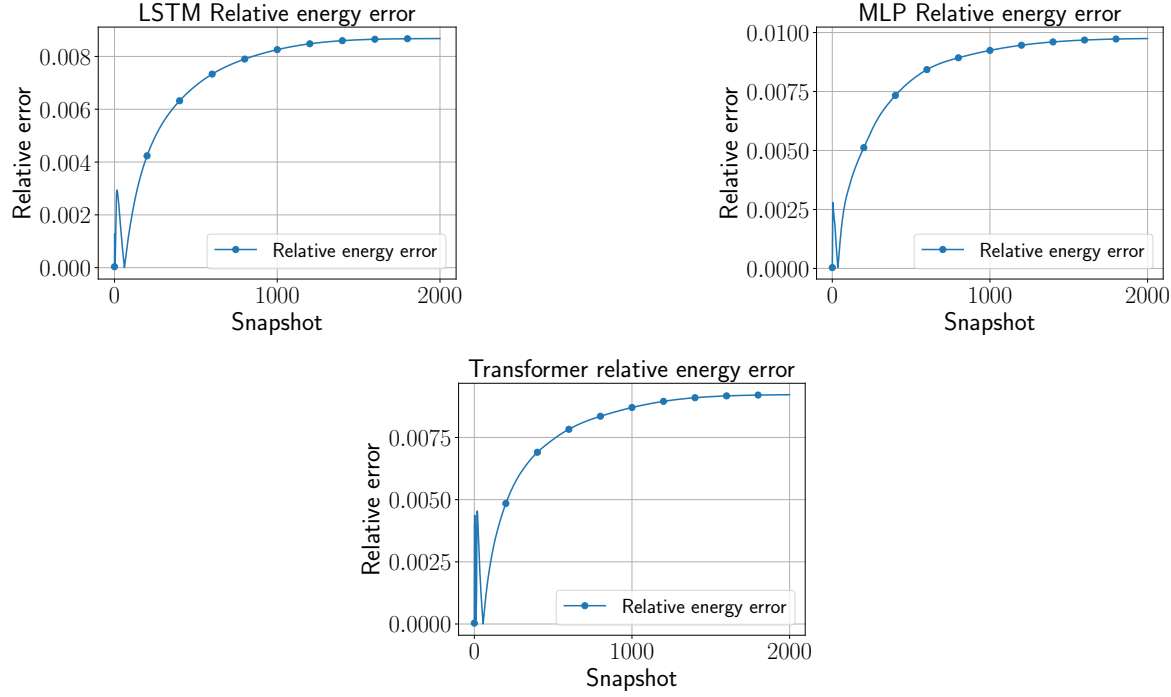


Figure 14: Error (FOM vs ROM) in terms of energy: on the left LSTM, in the center MLP, on the right Transformer.

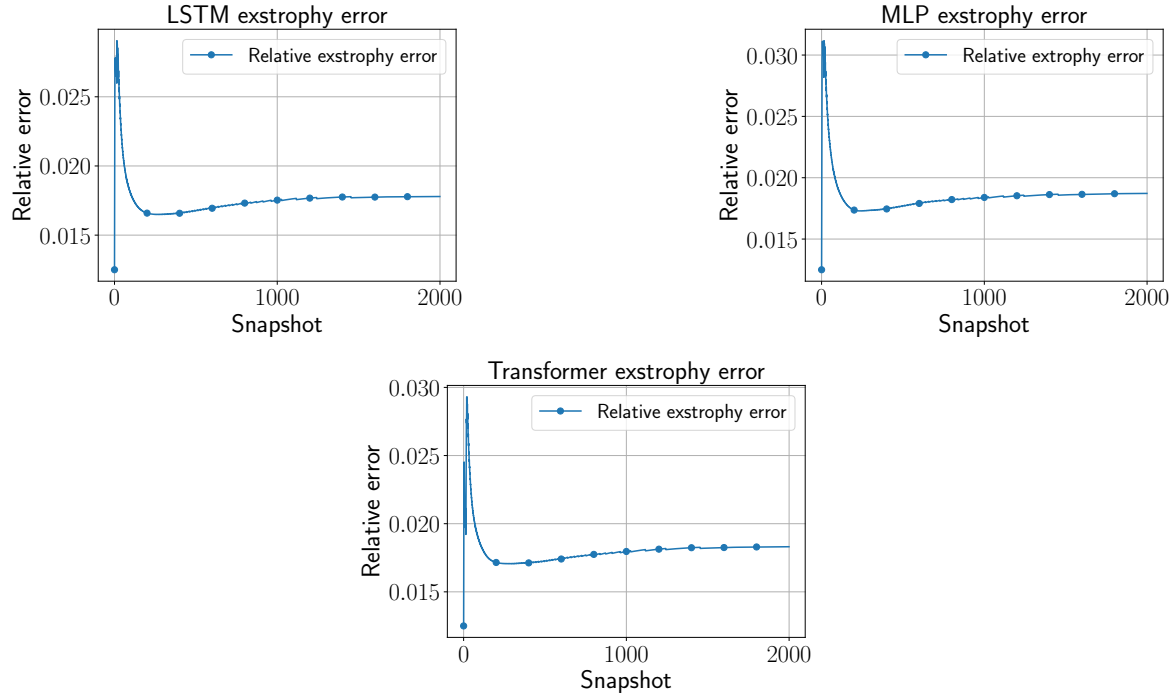


Figure 15: Error (FOM vs ROM) in terms of extropy: on the left LSTM, in the center MLP, on the right Transformer.

In terms of energy and extropy, the three configurations exhibit similar performance; however, the LSTM-based model demonstrates a slight advantage over the others.

All the results are summarized in the Table ??.

Table 1: Summary of relative errors between the FOM and ROM across different neural network architectures.

	<b>LSTM</b>	<b>MLP</b>	<b>Transformer</b>
<i>Error: FOM vs ROM (Mode variations)</i>			
Velocity	0.7%	0.8%	0.8%
Pressure	6.0%	6.0%	6.0%
Turbulent viscosity	2.0%	10.0%	7.0%
<i>Error: FOM vs ROM (Time variations)</i>			
Velocity	0.7%	0.8%	0.8%
Pressure	6.0%	6.0%	6.0%
Turbulent viscosity	4.0%	14.0%	9.0%
<i>Global Errors</i>			
Energy	0.7%	0.8%	0.8%
Enstrophy	1.7%	1.8%	1.8%

## 4 Conclusions and outlooks

This work introduces a novel hybrid framework that combines projection-based ROM with data-driven approaches for the treatment of turbulent viscosity. Specifically, the reduced order models for the velocity and pressure variables have been constructed following a “discretize-then-project” strategy ensuring full consistency with the underlying discrete formulation of the incompressible Navier–Stokes equations. At the same time, the turbulent viscosity field has been reconstructed through machine learning techniques, enabling a flexible and efficient integration of physical and data-driven components within the reduced framework.

A central outcome of this study concerns the role of the neural network architecture adopted for the modeling of turbulent viscosity within the reduced-order setting. Based on the numerical results, the LSTM architecture shows more reliable performance than the MLP and Transformer models for the present test case. This behavior suggests that explicitly accounting for temporal correlations plays an important role when modeling unsteady turbulent dynamics, particularly in situations where the evolution of the closure term depends on the recent flow history.

The hybrid model was tested by comparing reduced-order results with the corresponding full-order simulations. For the configuration considered in this work, the reduced model captures the main characteristics of the flow evolution. This indicates that the combination of projection-based reduction and data-driven modeling can be used for turbulent viscosity prediction in this setting. Additional test cases will be required to evaluate how the approach performs for other flow conditions and geometries.

## Acknowledgments

We acknowledge the financial support under the National Recovery and Resilience Plan (NRRP), Mission 4, Component 2, Investment 1.1, Call for tender No. 1409 published on 14.9.2022 by the Italian Ministry of University and Research (MUR), funded by the European Union – NextGenerationEU– Project Title ROMEU – CUP P2022FEZS3 - Grant Assignment Decree No. 1379 adopted on 01/09/2023 by the Italian Ministry of Ministry of University and Research (MUR) and acknowledges the financial support by the European Union (ERC, DANTE, GA-101115741). Views and opinions expressed are however those of the author(s) only and do not necessarily reflect those of the European Union or the European Research Council Executive Agency. Neither the European Union nor the granting authority can be held responsible for them.

## References

- [1] P. Benner, S. Gugercin, and K. Willcox, “A survey of Projection-Based Model Reduction Methods for Parametric Dynamical Systems,” *SIAM Review*, vol. 57, no. 4, p. 483–531, 2015.
- [2] G. Rozza, M. Malik, N. Demo, M. Tezzele, M. Girfoglio, G. Stabile, and A. Mola, “Advances in reduced order methods for parametric industrial problems in computational fluid dynamics,” p. 59 – 76, 2020.
- [3] K. Willcox and J. Peraire, “Balanced Model Reduction via the Proper Orthogonal Decomposition,” *AIAA Journal*, vol. 40, no. 11, p. 2323–2330, 2002.
- [4] C. W. ROWLEY, “Model Reduction for fluids, using balanced Proper Orthogonal Decomposition,” *International Journal of Bifurcation and Chaos*, vol. 15, no. 03, p. 997–1013, 2005.
- [5] T. Bui-Thanh, K. Willcox, O. Ghattas, and B. van Bloemen Waanders, “Goal-oriented, model-constrained optimization for reduction of large-scale systems,” *Journal of Computational Physics*, vol. 224, no. 2, p. 880–896, 2007.
- [6] S. S. Ravindran, “A reduced-order approach for optimal control of fluids using proper orthogonal decomposition,” *International Journal for Numerical Methods in Fluids*, vol. 34, no. 5, p. 425–448, 2000.
- [7] G. Rozza, D. B. P. Huynh, and A. T. Patera, “Reduced Basis Approximation and a Posteriori Error Estimation for Affinely Parametrized Elliptic Coercive Partial Differential Equations: Application to Transport and Continuum Mechanics,” *Archives of Computational Methods in Engineering*, vol. 15, no. 3, p. 229–275, 2008.
- [8] K. Veroy, C. Prud’homme, and A. T. Patera, “Reduced-basis approximation of the viscous Burgers equation: rigorous a posteriori error bounds,” *Comptes Rendus. Mathématique*, vol. 337, no. 9, p. 619–624, 2003.
- [9] J. S. Hesthaven, G. Rozza, and B. Stamm, *Certified Reduced Basis Methods for Parametrized Partial Differential Equations*. Springer International Publishing, 2016.
- [10] C. Prud’homme, D. V. Rovas, K. Veroy, L. Machiels, Y. Maday, A. T. Patera, and G. Turinici, “Reliable Real-Time Solution of Parametrized Partial Differential Equations: Reduced-Basis Output Bound Methods,” *Journal of Fluids Engineering*, vol. 124, no. 1, p. 70–80, 2001.
- [11] P. J. SCHMID, “Dynamic mode decomposition of numerical and experimental data,” *Journal of Fluid Mechanics*, vol. 656, p. 5–28, 2010.
- [12] J. N. Kutz, S. L. Brunton, B. W. Brunton, and J. L. Proctor, *Dynamic Mode Decomposition: Data-Driven Modeling of Complex Systems*. Society for Industrial and Applied Mathematics, 2016.
- [13] G. Tissot, L. Cordier, N. Benard, and B. R. Noack, “Model reduction using Dynamic Mode Decomposition,” *Comptes Rendus. Mécanique*, vol. 342, no. 6–7, p. 410–416, 2014.
- [14] P. Holmes, J. L. Lumley, G. Berkooz, and C. W. Rowley, *Turbulence, Coherent Structures, Dynamical Systems and Symmetry*. Cambridge University Press, 2012.
- [15] L. Sirovich, “Turbulence and the dynamics of coherent structures. i. coherent structures,” *Quarterly of Applied Mathematics*, vol. 45, no. 3, p. 561–571, 1987.
- [16] D. Galbally, K. Fidkowski, K. Willcox, and O. Ghattas, “Non-linear model reduction for uncertainty quantification in large-scale inverse problems,” *International Journal for Numerical Methods in Engineering*, vol. 81, no. 12, p. 1581–1608, 2009.
- [17] S. Chaturantabut and D. C. Sorensen, “Nonlinear Model Reduction via Discrete Empirical Interpolation,” *SIAM Journal on Scientific Computing*, vol. 32, no. 5, p. 2737–2764, 2010.

- [18] D. Amsallem, M. J. Zahr, and C. Farhat, “Nonlinear model order reduction based on local reduced-order bases,” *International Journal for Numerical Methods in Engineering*, vol. 92, no. 10, p. 891–916, 2012.
- [19] A. Quarteroni, A. Manzoni, and F. Negri, *Reduced Basis Methods for Partial Differential Equations*. Springer International Publishing, 2016.
- [20] M. Bergmann, C.-H. Bruneau, and A. Iollo, “Enablers for robust POD models,” *Journal of Computational Physics*, vol. 228, no. 2, p. 516–538, 2009.
- [21] G. Berkooz, P. Holmes, and J. L. Lumley, “The Proper Orthogonal Decomposition in the Analysis of Turbulent Flows,” *Annual Review of Fluid Mechanics*, vol. 25, no. 1, p. 539–575, 1993.
- [22] R. Chakir and Y. Maday, “A two-grid finite-element/reduced basis scheme for the approximation of the solution of parameter dependent PDE,” in *9e Colloque national en calcul des structures*, (Giens, France), CSMA, May 2009.
- [23] *Reduced Order Methods for Modeling and Computational Reduction*. Springer International Publishing, 2014.
- [24] S. Lorenzi, A. Cammi, L. Luzzi, and G. Rozza, “POD-Galerkin method for finite volume approximation of Navier–Stokes and RANS equations,” *Computer Methods in Applied Mechanics and Engineering*, vol. 311, p. 151–179, 2016.
- [25] G. Stabile and G. Rozza, “Finite volume POD-Galerkin stabilised reduced order methods for the parametrised incompressible Navier–Stokes equations,” *Computers & Fluids*, vol. 173, p. 273–284, 2018.
- [26] K. Carlberg, Y. Choi, and S. Sargsyan, “Conservative model reduction for finite-volume models,” *Journal of Computational Physics*, vol. 371, p. 280–314, 2018.
- [27] B. Haasdonk and M. Ohlberger, “Reduced basis method for finite volume approximations of parametrized linear evolution equations,” *ESAIM: Mathematical Modelling and Numerical Analysis*, vol. 42, no. 2, p. 277–302, 2008.
- [28] R. Eymard, T. Gallouët, and R. Herbin, *Finite volume methods*, p. 713–1018. Elsevier, 2000.
- [29] *Finite Volume Method - Powerful Means of Engineering Design*. InTech, 2012.
- [30] A. Syrakos, S. Varchanis, Y. Dimakopoulos, A. Goulas, and J. Tsamopoulos, “A critical analysis of some popular methods for the discretisation of the gradient operator in finite volume methods,” *Physics of Fluids*, vol. 29, no. 12, 2017.
- [31] V. H. K, *An Introduction to computational fluid dynamics : the finite volume method / H.K. Versteeg and W. Malalasekera*. Harlow [etc.]: Pearson, 2. ed. ed., 2007.
- [32] C. Fletcher, *Computational Techniques for Fluid Dynamics 1. Computational Techniques for Fluid Dynamics*. Springer Berlin Heidelberg, 1991.
- [33] J. Ferziger and M. Peric, *Computational Methods for Fluid Dynamics*. Springer Berlin Heidelberg, 2012.
- [34] F. H. Harlow and J. E. Welch, “Numerical Calculation of Time-Dependent Viscous Incompressible Flow of Fluid with Free Surface,” *The Physics of Fluids*, vol. 8, no. 12, p. 2182–2189, 1965.
- [35] O. V. Vasilyev, “High Order Finite Difference Schemes on Non-uniform Meshes with Good Conservation Properties,” *Journal of Computational Physics*, vol. 157, no. 2, p. 746–761, 2000.
- [36] S. V. Patankar, *Numerical Heat Transfer and Fluid Flow*. CRC Press, 2018.
- [37] M. Piller and E. Stalio, “Finite-volume compact schemes on staggered grids,” *Journal of Computational Physics*, vol. 197, no. 1, p. 299–340, 2004.

- [38] M. Perić, R. Kessler, and G. Scheuerer, “Comparison of finite-volume numerical methods with staggered and colocated grids,” *Computers & Fluids*, vol. 16, no. 4, p. 389–403, 1988.
- [39] Y. Zang, R. L. Street, and J. R. Koseff, “A Non-staggered Grid, Fractional Step Method for Time-Dependent Incompressible Navier-Stokes Equations in Curvilinear Coordinates,” *Journal of Computational Physics*, vol. 114, no. 1, p. 18–33, 1994.
- [40] R. Jia, M. S. Kamel, C. Wu, and B. Agrawal, “Ansys Fluent HPC for Large-Scale CFD Simulations,” in *AIAA SCITECH 2025 Forum*, American Institute of Aeronautics and Astronautics, 2025.
- [41] F. Rezaei and M. Paraschivoiu, “Evaluating roof-mounted VAWT performance with CFD for various building shapes, boundary layer flows, and location scenarios,” *Transactions of the Canadian Society for Mechanical Engineering*, vol. 49, no. 2, p. 350–367, 2025.
- [42] I. Kalashnikova and M. Barone, “Stable and Efficient Galerkin Reduced Order Models for Non-Linear Fluid Flow,” in *6th AIAA Theoretical Fluid Mechanics Conference*, American Institute of Aeronautics and Astronautics, 2011.
- [43] A. Iollo, S. Lanteri, and J.-A. Désidéri, “Stability properties of POD-Galerkin approximations for the compressible Navier-Stokes equations,” *Theoretical and Computational Fluid Dynamics*, vol. 13, no. 6, p. 377–396, 2000.
- [44] M. J. Balajewicz, E. H. Dowell, and B. R. Noack, “Low-dimensional modelling of high-Reynolds-number shear flows incorporating constraints from the Navier–Stokes equation,” *Journal of Fluid Mechanics*, vol. 729, p. 285–308, 2013.
- [45] M. Balajewicz, I. Tezaur, and E. Dowell, “Minimal subspace rotation on the Stiefel manifold for stabilization and enhancement of projection-based reduced order models for the compressible Navier–Stokes equations,” *Journal of Computational Physics*, vol. 321, p. 224–241, 2016.
- [46] X. MA and G. E. KARNIADAKIS, “A low-dimensional model for simulating three-dimensional cylinder flow,” *Journal of Fluid Mechanics*, vol. 458, p. 181–190, 2002.
- [47] B. Sanderse, “Non-linearly stable reduced-order models for incompressible flow with energy-conserving finite volume methods,” *Journal of Computational Physics*, vol. 421, p. 109736, 2020.
- [48] C. M. Rie and W. L. Chow, “Numerical study of the turbulent flow past an airfoil with trailing edge separation,” *AIAA Journal*, vol. 21, no. 11, p. 1525–1532, 1983.
- [49] F. Ballarin, A. Manzoni, A. Quarteroni, and G. Rozza, “Supremizer stabilization of POD–Galerkin approximation of parametrized steady incompressible Navier–Stokes equations,” *International Journal for Numerical Methods in Engineering*, vol. 102, no. 5, p. 1136–1161, 2014.
- [50] I. Akhtar, A. H. Nayfeh, and C. J. Rabbens, “On the stability and extension of reduced-order Galerkin models in incompressible flows: A numerical study of vortex shedding,” *Theoretical and Computational Fluid Dynamics*, vol. 23, no. 3, p. 213–237, 2009.
- [51] B. R. NOACK, P. PAPAS, and P. A. MONKEWITZ, “The need for a pressure-term representation in empirical Galerkin models of incompressible shear flows,” *Journal of Fluid Mechanics*, vol. 523, p. 339–365, 2005.
- [52] A. Caiazzo, T. Iliescu, V. John, and S. Schyschlowa, “A numerical investigation of velocity–pressure reduced order models for incompressible flows,” *Journal of Computational Physics*, vol. 259, p. 598–616, 2014.
- [53] K. Kean and M. Schnieer, “Error Analysis of Supremizer Pressure Recovery for POD based Reduced-Order Models of the Time-Dependent Navier-Stokes Equations,” *SIAM Journal on Numerical Analysis*, vol. 58, no. 4, p. 2235–2264, 2020.
- [54] P. Gresho and R. Sani, *Incompressible Flow and the Finite Element Method, Volume 1: Advection-Diffusion and Isothermal Laminar Flow*. Wiley, 2000.

[55] J.-G. Liu, J. Liu, and R. L. Pego, “Stable and accurate pressure approximation for unsteady incompressible viscous flow,” *Journal of Computational Physics*, vol. 229, no. 9, p. 3428–3453, 2010.

[56] S. Busto, G. Stabile, G. Rozza, and M. Vázquez-Cendón, “POD–Galerkin reduced order methods for combined Navier–Stokes transport equations based on a hybrid FV–FE solver,” *Computers & Mathematics with Applications*, vol. 79, no. 2, p. 256–273, 2020.

[57] S. Rubino, “Numerical Analysis of a Projection-Based Stabilized POD-ROM for Incompressible Flows,” *SIAM Journal on Numerical Analysis*, vol. 58, no. 4, p. 2019–2058, 2020.

[58] J. Novo and S. Rubino, “Error Analysis of Proper Orthogonal Decomposition Stabilized Methods for Incompressible Flows,” *SIAM Journal on Numerical Analysis*, vol. 59, no. 1, p. 334–369, 2021.

[59] V. DeCaria, T. Iliescu, W. Layton, M. McLaughlin, and M. Schneier, “An Artificial Compression Reduced Order Model,” *SIAM Journal on Numerical Analysis*, vol. 58, no. 1, p. 565–589, 2020.

[60] S. K. Star, B. Sanderse, G. Stabile, G. Rozza, and J. Degroote, “Reduced order models for the incompressible Navier–Stokes equations on collocated grids using a ‘discretize-then-project’ approach,” 2020.

[61] I. Kalashnikova and M. F. Barone, “Efficient non-linear proper orthogonal decomposition/Galerkin reduced order models with stable penalty enforcement of boundary conditions,” *International Journal for Numerical Methods in Engineering*, vol. 90, no. 11, p. 1337–1362, 2012.

[62] S. Sirisup and G. Karniadakis, “Stability and accuracy of periodic flow solutions obtained by a POD-penalty method,” *Physica D: Nonlinear Phenomena*, vol. 202, no. 3–4, p. 218–237, 2005.

[63] G. Stabile, S. Hijazi, A. Mola, S. Lorenzi, and G. Rozza, “POD–Galerkin reduced order methods for CFD using Finite Volume Discretisation: vortex shedding around a circular cylinder,” *Communications in Applied and Industrial Mathematics*, vol. 8, no. 1, p. 210–236, 2017.

[64] S. Ullmann and J. Lang, *POD–Galerkin Modeling and Sparse-Grid Collocation for a Natural Convection Problem with Stochastic Boundary Conditions*, ISBN = 9783319045375, p. 295–315. Springer International Publishing, 2014.

[65] L. Fick, Y. Maday, A. T. Patera, and T. Taddei, “A stabilized POD model for turbulent flows over a range of Reynolds numbers: Optimal parameter sampling and constrained projection,” *Journal of Computational Physics*, vol. 371, p. 214–243, 2018.

[66] K. Carlberg, C. Farhat, J. Cortial, and D. Amsallem, “The GNAT method for nonlinear model reduction: Effective implementation and application to computational fluid dynamics and turbulent flows,” *Journal of Computational Physics*, vol. 242, p. 623–647, 2013.

[67] K. Lee and K. T. Carlberg, “Model reduction of dynamical systems on nonlinear manifolds using deep convolutional autoencoders,” *Journal of Computational Physics*, vol. 404, p. 108973, 2020.

[68] A. Placzek, D.-M. Tran, and R. Ohayon, “A nonlinear POD–Galerkin reduced-order model for compressible flows taking into account rigid body motions,” *Computer Methods in Applied Mechanics and Engineering*, vol. 200, no. 49–52, p. 3497–3514, 2011.

[69] A. Ivagnes, G. Stabile, A. Mola, T. Iliescu, and G. Rozza, “Hybrid data-driven closure strategies for reduced order modeling,” *Applied Mathematics and Computation*, vol. 448, p. 127920, 2023.

[70] J. Baiges, R. Codina, and S. Idelsohn, “Explicit reduced-order models for the stabilized finite element approximation of the incompressible Navier–Stokes equations,” *International Journal for Numerical Methods in Fluids*, vol. 72, no. 12, p. 1219–1243, 2013.

[71] C. Klaij, “On the stabilization of finite volume methods with co-located variables for incompressible flow,” *Journal of Computational Physics*, vol. 297, p. 84–89, 2015.

[72] A. Date, “Solution of Navier–Stokes equations on non-staggered grid,” *International Journal of Heat and Mass Transfer*, vol. 36, no. 7, p. 1913–1922, 1993.

- [73] R. Issa, “Solution of the implicitly discretised fluid flow equations by operator-splitting,” *Journal of Computational Physics*, vol. 62, no. 1, p. 40–65, 1986.
- [74] E. Komen, E. Frederix, T. Coppen, V. D’Alessandro, and J. Kuerten, “Analysis of the numerical dissipation rate of different Runge–Kutta and velocity interpolation methods in an unstructured collocated finite volume method in OpenFOAM®,” *Computer Physics Communications*, vol. 253, p. 107145, 2020.
- [75] C. Hirsch, *Numerical Computation of Internal and External Flows: The Fundamentals of Computational Fluid Dynamics*. Butterworth-Heinemann, 2007.
- [76] V. Kazemi-Kamyab, A. van Zuijlen, and H. Bijl, “Analysis and application of high order implicit Runge–Kutta schemes to collocated finite volume discretization of the incompressible Navier–Stokes equations,” *Computers & Fluids*, vol. 108, p. 107–115, 2015.
- [77] V. Vuorinen, J.-P. Keskinen, C. Duwig, and B. Boersma, “On the implementation of low-dissipative Runge–Kutta projection methods for time dependent flows using OpenFOAM®,” *Computers & Fluids*, vol. 93, p. 153–163, 2014.
- [78] C. Canuto, M. Hussaini, A. Quarteroni, and T. Zang, *Spectral Methods: Fundamentals in Single Domains*. Scientific Computation, Springer Berlin Heidelberg, 2007.
- [79] A. J. Chorin, “Numerical solution of the Navier–Stokes equations,” *Mathematics of Computation*, vol. 22, no. 104, p. 745–762, 1968.
- [80] Y. Morinishi, T. Lund, O. Vasilyev, and P. Moin, “Fully Conservative Higher Order Finite Difference Schemes for Incompressible Flow,” *Journal of Computational Physics*, vol. 143, no. 1, p. 90–124, 1998.
- [81] F. N. Felten and T. S. Lund, “Kinetic energy conservation issues associated with the collocated mesh scheme for incompressible flow,” *Journal of Computational Physics*, vol. 215, no. 2, p. 465–484, 2006.

## Appendix

The numerical simulations were performed using the ITHACA-FV library based on OpenFOAM. Specifically, the unsteady Navier–Stokes cases were set up using the solver available in the repository.

The hyperparameters presented in Table 2 define the technical configuration for the non-intrusive, data-driven component of the hybrid framework. While velocity and pressure are resolved through intrusive Galerkin projection, these network architectures are designed to reconstruct the temporal evolution of the turbulent viscosity coefficients.

To ensure a robust learning process for the 3D turbulent lid-driven cavity case, the dataset was partitioned into 1,800 training samples and 200 validation samples from a total of 2,000 high-fidelity snapshots. All models utilized the Adam optimizer and Mean Squared Error (MSE) loss function, which are standard for regressing modal coefficients in fluid dynamics applications. Numerical stability across the different architectures was maintained by applying a StandardScaler to normalise both input (velocity and pressure coefficients) and output (turbulent viscosity coefficients) sequences.

For the sequence-based models (LSTM and Transformer), a lookback window of 15 time steps was adopted. This choice allows the networks to incorporate information from recent temporal history when predicting the turbulent viscosity coefficients, which is relevant for representing the time-dependent behavior observed in the unsteady turbulent flow.

Table 2: Hyperparameters of the Neural Network architectures used in this study.

Hyperparameters	LSTM	MLP	Transformer
<i>General Training</i>			
Epochs	1200	1200	1000
Training Samples	1800	1800	1800
Validation Samples	200	200	200
Batch Size	64	64	64
Optimizer	Adam	Adam	Adam
Loss Function	MSE	MSE	MSE
Learning Rate	$2 \times 10^{-5}$	$3 \times 10^{-5}$	$9 \times 10^{-5}$
Normalization	StandardScaler	StandardScaler	StandardScaler
<i>Architecture Specifics</i>			
Lookback Window	15	—	15
Hidden Layers	4	4	—
<i>Transformer Specifics</i>			
Attention Heads	—	—	4
Feed Forward Dim	—	—	128
Dropout	—	—	0.1
Layer Norm $\epsilon$	—	—	$1 \times 10^{-6}$

The internal configurations adopted for the two main neural network models considered in this study, LSTM network and the Multilayer MLP, are reported in Table 3. Both architectures are employed within the non-intrusive component of the hybrid framework and are used to model the temporal evolution of the turbulent viscosity coefficients in the reduced-order space.

The LSTM model is designed to exploit temporal dependencies and "context" through its gated memory mechanism. To achieve this, the architecture utilizes a hierarchical recurrent structure: the first layer (64 units) is configured to Return Sequences, allowing the model to pass the temporal information from the input lookback window to the subsequent 32-unit LSTM layer. This is followed by a dense layer with ReLU activation to model complex nonlinearities before reaching the linear output layer, which predicts the reduced turbulent viscosity coefficients ( $r_{nut}$ ).

The MLP architecture, by contrast, consists of a sequence of fully connected layers without explicit temporal recurrence. The network starts with a dense layer of 128 units, intended to capture global relationships in the input features. To limit overfitting during training on high-fidelity LES data, a Dropout layer with a rate of 0.2 is included. As in the LSTM case, the network terminates with a linear output layer, which produces the predicted coefficient vector  $Y_{dim}$ .

Table 3: Layer-wise architecture details for the LSTM and MLP models.

Model	Layer	Output Shape	Parameters / Config
<b>LSTM</b>	1. LSTM (64 units)	$15 \times 64$	Return Sequences
	2. LSTM (32 units)	32	No Return Sequences
	3. Dense (32 units)	32	ReLU Activation
	4. Output (Dense)	$r_{nut}$	Linear Activation
<b>MLP</b>	1. Dense (128 units)	128	ReLU
	2. Dropout	128	Rate = 0.2
	3. Dense (64 units)	64	ReLU
	4. Output (Dense)	$Y_{dim}$	Linear Activation